

SODAs: Sparse Optimization for the Discovery of Differential and Algebraic Equations

Manu Jayadharan¹, Christina Catlett¹, Arthur N. Montanari², and Niall M. Mangan^{1,*}

¹Department of Engineering Sciences and Applied Mathematics, Northwestern University, Evanston, IL 60208, USA

²Department of Physics and Astronomy, Northwestern University, Evanston, IL 60208, USA

*niall.mangan@northwestern.edu

ABSTRACT

Differential-algebraic equations (DAEs) integrate ordinary differential equations (ODEs) with algebraic constraints, providing a fundamental framework for developing models of dynamical systems characterized by timescale separation, conservation laws, and physical constraints. While sparse optimization has revolutionized model development by allowing data-driven discovery of parsimonious models from a library of possible equations, existing approaches for dynamical systems assume DAEs can be reduced to ODEs by eliminating variables before model discovery. This assumption limits the applicability of such methods to DAE systems with unknown constraints and time scales. We introduce Sparse Optimization for Differential-Algebraic Systems (SODAs), a data-driven method for the identification of DAEs in their explicit form. By discovering the algebraic and dynamic components sequentially without prior identification of the algebraic variables, this approach leads to a sequence of convex optimization problems and has the advantage of discovering interpretable models that preserve the structure of the underlying physical system. To this end, SODAs improves numerical stability when handling high correlations between library terms—caused by near-perfect algebraic relationships—by iteratively refining the conditioning of the candidate library. We demonstrate the performance of our method on biological, mechanical, and electrical systems, showcasing its robustness to noise in both simulated time series and real-time experimental data.

1 Introduction

Data-driven discovery of dynamical models of complex systems promises to rapidly accelerate our understanding, from learning new equations governing cellular biomechanics [1] to the automatic generation of control models for robotics [2, 3]. A major challenge of many complex dynamical systems is the separation of timescales and the integration of physical constraints and conservation laws. Timescale separation is ubiquitous in complex biological and physical systems, from metabolic networks to multi-body robotics and power grids. Even in well-studied systems such as those following mass-action kinetics and deterministic Newtonian physics, numerical simulation and parameter estimation are challenging due to the inherent stiffness of such systems [4–6]. In this context, model selection is an even greater challenge as the structural form of the model, including its conservation laws and relevant timescales, may be unknown. In this work, we propose a method for data-driven discovery of complex systems by designing sparse-model selection within a differential-algebraic equation (DAE) framework, where conservation laws and quasi-steady-state equations are learned from time-series data as algebraic equations.

Model identification or selection focuses on the general challenge of discovering the functional form of a model using data. For many dynamical systems—including those following mass-action kinetics or electromechanical conservation laws—it is reasonable to enumerate a library of possible interaction terms or candidate functions $\Theta = \{\theta_1(\mathbf{x}), \dots, \theta_J(\mathbf{x})\}$, each representing a meaningful physical quantity as a function of the system state $\mathbf{x}(t)$. The key challenge is to downselect the most suitable subset of terms from this library. For example, a system of differential equations can often be described using a linear combination of nonlinear functions: $\dot{x}_i = \sum_{j=1}^J p_j^i \theta_j(\mathbf{x})$, for each state variable $i = 1, \dots, d$, where p_j^i are parameters. Popular candidates for Θ include monomial bases, rational functions, and Fourier bases. There exist several methods to identify nonzero coefficients $p_j^i \neq 0$, thereby learning which functions $\theta_j(\mathbf{x})$ influence the dynamics of state x_i , including Bayesian variable selection [7], best subset selection [8, 9], and sparse regression [10]. Of these, sparse regression has gained popularity due to its relative simplicity and low computational cost. Among the best known examples, Sparse Optimization for Nonlinear Dynamics (SINDy) finds a parsimonious model by minimizing

$$L_i(\mathbf{p}^i) = \sum_{r=1}^N \|\dot{x}_i(t_r) - \sum_{j=1}^J p_j^i \theta_j(x_1(t_r), x_2(t_r), \dots, x_d(t_r))\|^2 + \alpha \|\mathbf{p}^i\|_1, \quad i = 1, \dots, d, \quad (1)$$

where α controls the weight of the penalty term enforcing sparsity and N is the number of data samples, and \mathbf{p}^i is a vector

of parameters for the i^{th} state equation. If all states x_i are measured and the derivatives \dot{x}_i can be measured or numerically estimated, then the model is linear with respect to the unknown parameters and hence minimization can be performed through alternating least-squares and hard-thresholding or regularized approaches such as LASSO [11], Elastic-net [12], or SR3 [13]. Prior work has addressed the challenge of applying SINDy on noisy data, including smoothing splines [14], interpolation [15], and integral formulations of sparse regression (e.g., weak SINDy [16, 17], D-SINDy [18], etc.).

Such sparse regression methods are effective for applications in which the differential variables are identified, all variables are measured, and the model is linear in the unknown parameters \mathbf{p} . However, for complex systems described by DAEs, one or more of these assumptions break down. Recent approaches have used nonlinear optimization for sparse-model selection in systems with partial measurements [19–22]. Yet, they rely on the assumption that the system is well-described by ordinary differential equations (ODEs) and do not explicitly incorporate algebraic constraints. Other groups have focused on model discovery for DAE systems but only when the conservation laws, network topology, or other algebraic constraints are known [23–25]. Some DAEs can be converted to ODEs through substitution of the algebraic equations, reducing the dimension of state space and producing ODEs with rational functions on the right-hand side. Implicit-SINDy [26], and the more computationally efficient parallel implicit SINDy (PI-SINDy) [27], have demonstrated sparse-model selection for ODEs with rational functions. However, these methods require that the differential variables are identified *a priori* (see Section 2.2 for further discussion). A related concept was introduced in [28], where principal component analysis (PCA) is used to eliminate correlated features from the library by retaining only those with the highest loadings in the first few principal components. However, this approach does not necessarily ensure a compact library, as the principal components may have uniformly distributed loadings unless a sparse PCA method is applied. No existing methods address the case where all states are measured, but the identity of the differential and algebraic variables is unknown, and the constraints must be identified.

In this paper, we propose Sparse Optimization for Differential-Algebraic Systems (SODAs), a novel approach for discovering DAE systems by sequentially identifying the algebraic equations and the differential equations. First, we iteratively identify algebraic relationships while partially parallelizing the optimization. Once these relationships are discovered, we refine the candidate function library to mitigate multicollinearity induced by algebraic relationships. Next, the dynamic component of the DAE system is discovered using the refined candidate function library and a selection of existing methods for ODE discovery ([10, 16, 29, 30]). This sequential approach improves the condition number of the library by eliminating redundant terms and restricts the challenge posed by noisy numerical derivatives in the ODE discovery phase. We employ a singular value decomposition (SVD) analysis of the candidate library as a guiding tool to determine the stopping criteria for the refinement process under high-noise conditions. The performance of our method is illustrated using numerous DAE systems, including chemical reaction networks (CRNs), multi-body mechanical systems, and power grids.

The paper is organized as follows. Section 2 provides a brief introduction to DAEs and the challenges associated with the existing SINDy framework for their discovery. The SODAs method is presented in Section 3, together with a detailed algorithm, a Python implementation of SODAs (called `DaeFinder`), and an example application to a simple CRN. In Section 4, we demonstrate: 1) successful rediscovery of the DAEs used to simulate time series of chemical concentrations in CRNs, 2) discovery of a reduced coordinate system and subsequent discovery of ODEs from pixel data obtained from real-time footage of experiments and video recordings of animated single and double pendulums, and 3) rediscovery of the DAEs used in power grid modeling for 3 IEEE benchmark cases. Finally, in Section 5, we address various challenges associated with our method and discuss possible improvements.

2 Background: DAEs and existing SINDy frameworks

2.1 Differential-Algebraic Equations

In the types of physical systems in which we are interested, DAEs commonly arise from quasi-steady state approximations, conservation laws, and physical constraints, as seen in the modeling of chemical reactions, power grids, and multi-body systems [31]. When DAEs arise from quasi-steady state approximations [32, 33], where fast variables are assumed to reach equilibrium instantaneously relative to other variables operating in slower dynamics, it is often challenging to identify which variables are in quasi-steady state and are, therefore, algebraic rather than differential.

Let $\mathbf{x}(t) = (\mathbf{y}(t), \mathbf{z}(t))$ represent the state variables in the dynamical system, such that $\mathbf{y} = [y_1, \dots, y_m]^T \in C^c([0, T], \mathbb{R}^m)$ and $\mathbf{z} = [z_1, \dots, z_{d-m}]^T \in C^0([0, T], \mathbb{R}^{d-m})$. The following set of equations represents a system of DAEs in a semi-explicit form, where the algebraic constraints can be separated from the differential operator:

$$\mathbf{F}(\mathbf{y}, \dot{\mathbf{y}}, \ddot{\mathbf{y}}, \dots, \mathbf{z}, t) = 0, \quad (2)$$

$$\mathbf{G}(\mathbf{y}, \mathbf{z}, t) = 0, \quad (3)$$

where $\mathbf{F} = (f_1, \dots, f_m)$ and $\mathbf{G} = (g_1, \dots, g_{d-m})$ represent the differential and algebraic parts of the system, respectively. Note that time derivatives, up to order c , appear only in the differential state variables \mathbf{y} , while the algebraic variables \mathbf{z} are continuous

on $[0, T]$. DAEs can also be expressed in an implicit form, where the algebraic constraints are not separated, and our algorithm is designed to work for both forms. Note that the implicit form can be converted into a semi-explicit form and also that the latter form is often more natural for many applications, as it reflects the physical significance of the explicit algebraic constraints present in these contexts. We introduce our method using the semi-explicit form.

The DAE system (2)–(3) is well-posed depending on certain regularity conditions on \mathbf{F} and \mathbf{G} as well as the existence of compatible initial conditions \mathbf{x}_0 satisfying the algebraic constraints (3) (see [34], Chapter 2). DAEs can be further classified based on *indices* related to the easiness of conversion to an ODE system (via subsequent differentiation) or based on the complexity of the numerical solution. For a detailed analysis of the solvability of nonlinear DAE systems and their classification based on various indices, see [34] and [35]. We assume that the DAE system to be discovered from data is well-posed and that the state-space trajectories $\mathbf{x}(t)$ are smooth enough on the interval $[0, T]$.

A simple example of DAE system describes the chemical kinetics of an enzyme-mediated, irreversible reaction:

$$\frac{d[S]}{dt} = -k_1[E][S] + k_{-1}[ES], \quad (4)$$

$$\frac{d[P]}{dt} = k_{\text{cat}}[ES], \quad (5)$$

$$[E] + [ES] - E^{\text{tot}} = 0, \quad (6)$$

$$\frac{d[ES]}{dt} = (k_{-1} + k_{\text{cat}})[ES] - k_1[E][S] \approx 0, \quad (7)$$

where $[S]$, $[E]$, $[ES]$, $[P]$ are concentrations of substrate, enzyme, enzyme-substrate complex, and products of a CRN, respectively. The enzyme-substrate complex $[ES]$ can be assumed to be in quasi-steady state under many experimental conditions [36]. Once (7) is assumed to be in quasi-steady state, the differential variables are $[S]$ and $[P]$, and the algebraic variables are $[E]$ and $[ES]$.

2.2 Data-driven discovery of equivalent ODE systems

An approach previously explored is to discover the DAEs in their equivalent reduced ODE form. DAE systems of the form (2)–(3) can often be converted to a fully coupled ODE system:

$$\widehat{\mathbf{F}}(\mathbf{y}, \dot{\mathbf{y}}, \ddot{\mathbf{y}}, \dots, \mathbf{z}, t) = 0. \quad (8)$$

This reduction is performed regularly in many fields, including chemical, mechanical, and electrical engineering [31, 32], to reformulate models in a manner compatible with well-established techniques for ODEs, such as numerical solvers and control methods. The reduction involves eliminating state variables using algebraic constraints and can lead to more complicated expressions in (8) as compared to (2)–(3). For example, the system (4)–(7) can be reduced using (6) and (7) to eliminate $[E]$ and $[ES]$ resulting in

$$\frac{d[S]}{dt} = -\frac{k_1 k_{\text{cat}} E^{\text{tot}} [S]}{k_{-1} + k_{\text{cat}} + k_1 [S]}. \quad (9)$$

These are the canonical Michealis-Menten kinetics [37, 38]. More generally, DAE systems of monomial terms will generally reduce to the form

$$\frac{dx_i}{dt} = \frac{\sum_{j_n} p_{j_n}^i n_{j_n}^i(\mathbf{x})}{\sum_{j_d} p_{j_d} d_{j_d}^i(\mathbf{x})}, \quad i = 1, \dots, d, \quad (10)$$

where $n_{j_n}^i(\mathbf{x}), d_{j_d}^i(\mathbf{x}) \in \mathbb{R}[\mathbf{x}]$ are multivariate monomials of the state vector \mathbf{x} . This reduction to ODEs has resulted in rational functions of the state variables compared to the original set of equations, which only contained polynomial functions. Converting higher-index DAEs to a reduced ODEs can become more complicated, resulting in rational functions with nonlinear terms in both the numerator and denominator, even when the original DAE system consists of simple additive terms.

Although system (10) is now converted to an ODE form, the optimization cost (1) formulated in SINDy is not a convex problem anymore because the functions are rational and hence the model is not linear in the coefficients \mathbf{p} . This nonlinear optimization can be challenging due to various factors including non-convexity, poles of rational functions, and stability issues for techniques that use an ODE integration as part of the loss function evaluation. To address this issue, implicit-SINDy [26] reformulated the reduced ODEs of the form (10) as an implicit ODE and then applied sparse optimization. Expressed implicitly, (10) becomes

$$\frac{dx_i}{dt} \sum_j d_j^i(\mathbf{x}) - \sum_j n_j^i(\mathbf{x}) = 0, \quad i = 1, \dots, d. \quad (11)$$

In this implicit-SINDy framework, the candidate function library is augmented to be $\tilde{\Theta} = \{\dot{\mathbf{x}}\Theta, \Theta\}$, where $\dot{\mathbf{x}}\Theta$ denotes the set of all products of the state derivatives with the candidate functions. As a result, the library has $2J$ terms. The goal is then to satisfy equation (11) by finding a sparse vector in the nullspace of this augmented library $\tilde{\Theta}$, which can be achieved via the alternating direction method of multipliers (ADMM). Nonetheless, this method has some drawbacks, such as its sensitivity to noise when estimating the nullspace and its high data requirements.

The PI-SINDy method [27] improves upon the implicit-SINDy method by performing a partial combinatorial search: each library element in $\tilde{\Theta}$ is moved to the right-hand side of the ODE and standard sparse regression is applied assuming the moved term is part of the true equation. Solving the $2J$ convex, sparse linear regressions can also be parallelized in this approach. Notwithstanding, these implicit methods still require large amounts of data, and the robustness to noise is often insufficient for many practical applications. Specifically, PI-SINDy was applied to the Michaelis-Menten kinetics model using a large dataset consisting of 150,000 data points for training and testing, generated from 3,000 randomly sampled initial conditions. Despite this large volume of data, the method was shown to handle only Gaussian noise up to a magnitude of $\sigma = 0.04$ (Figure 3 in [27]), which corresponds to a noise level of less than 1% given that the initial condition for the chemical concentration ranged between 0 and 12.5 in magnitude.

2.3 Benefits and challenges of model discovery in the DAE framework

In addition to the high data quality requirements, a fundamental issue is that implicit-SINDy and PI-SINDy methods do not identify the algebraic variables and associated equations within a DAE system. The algebraic constraints in the DAEs typically carry physical significance related to physical constraints or quasi-steady-state approximations, and this intuitive meaning is lost in the equivalent ODE formulation. Creating an explicit system of ODEs in the form (8) can be complex, computationally intensive, or even impossible for higher-index DAE systems or when the algebraic constraints are not differentiable in time [39]. Furthermore, small parameter changes in the original DAE system often lead to distinct reduced ODE forms. Solving or discovering DAEs directly preserves the underlying structure of the problem. An additional benefit of identifying the algebraic relationships is that the library can be iteratively simplified by removing an algebraic variable for every algebraic equation discovered. Removal of terms with algebraic variables reduce multicollinearity among the candidate library terms due to the explicit algebraic constraints, improving the conditioning of the library. Consequently, the discovery of DAEs provides a more interpretable and computationally beneficial framing.

Discovering a DAE system in its semi-explicit form (2)–(3) also offers flexibility for numerical analysis and simulation. For example, in CRN applications, simulations are often carried out using ODE solvers designed for stiff systems; however, in applications involving high-index DAEs, solving a reduced ODE system can lead to numerical instability [34, 39, 40]. In these cases, single-step and multi-step methods for solving DAEs in their non-reduced forms are preferred [34, 35, 39–41]. By first discovering the DAE system in the semi-explicit form, the user can choose either to convert it to a reduced ODE or to keep the original semi-explicit form, depending on which numerical solvers are most appropriate. In comparison, converting a reduced ODE system back into a DAE system with explicit constraints is often not feasible.

To address all the issues discussed so far—including the interpretability of physical constraints, the numerical instabilities caused by perfect multicollinearity in the candidate library, and the adversarial effects of noise present in implicit ODE discovery—we propose the method SODAs. By separating the discovery of differential and algebraic equations, we directly identify the algebraic variables and equations and eliminate the impact of noisy derivatives on the discovery of algebraic equations. We can then utilize the knowledge gained from the discovered algebraic equations to better condition the library before attempting to discover differential equations.

3 Methods: Sparse Optimization for Differential-Algebraic Systems

In this section, we introduce our algorithm SODAs (Figure 1, Algorithm 1), and demonstrate how it can be used to discover DAEs in their explicit form (2)–(3). The core idea is to separate the discovery of the algebraic and dynamic state equations. `DaeFinder` is a Python implementation of SODAs that allows users to easily create popular candidate libraries relevant to many applications and efficiently implement various components of the SODAs algorithm. Through `DaeFinder`, SODAs iteratively identifies algebraic relationships, removes them from the library, and reduces multicollinearity within the library. After this process, SINDy is applied to discover the dynamic equations from the remaining library terms. We illustrate the application of SODAs using an example of a simple CRN (4)–(7) (Figure 1a).

Method formulation

Let $\mathbf{X} = [\mathbf{X}_1 \ \mathbf{X}_2 \ \dots \ \mathbf{X}_d]$ denote the $N \times d$ time-series data matrix, where each column \mathbf{X}_i contains possibly noisy measurements of the state x_i at time points $\{t_1 = 0, \dots, t_N = T\}$, such that $\mathbf{X}_{ij} \approx x_j(t_i)$. Note that the measurements $x_i(t)$ may also be obtained through transformations of the original state variables. However, for simplicity, throughout this paper, we assume that all states are directly observable with some measurement noise. SODAs is typically applied to DAE systems where the terms appearing

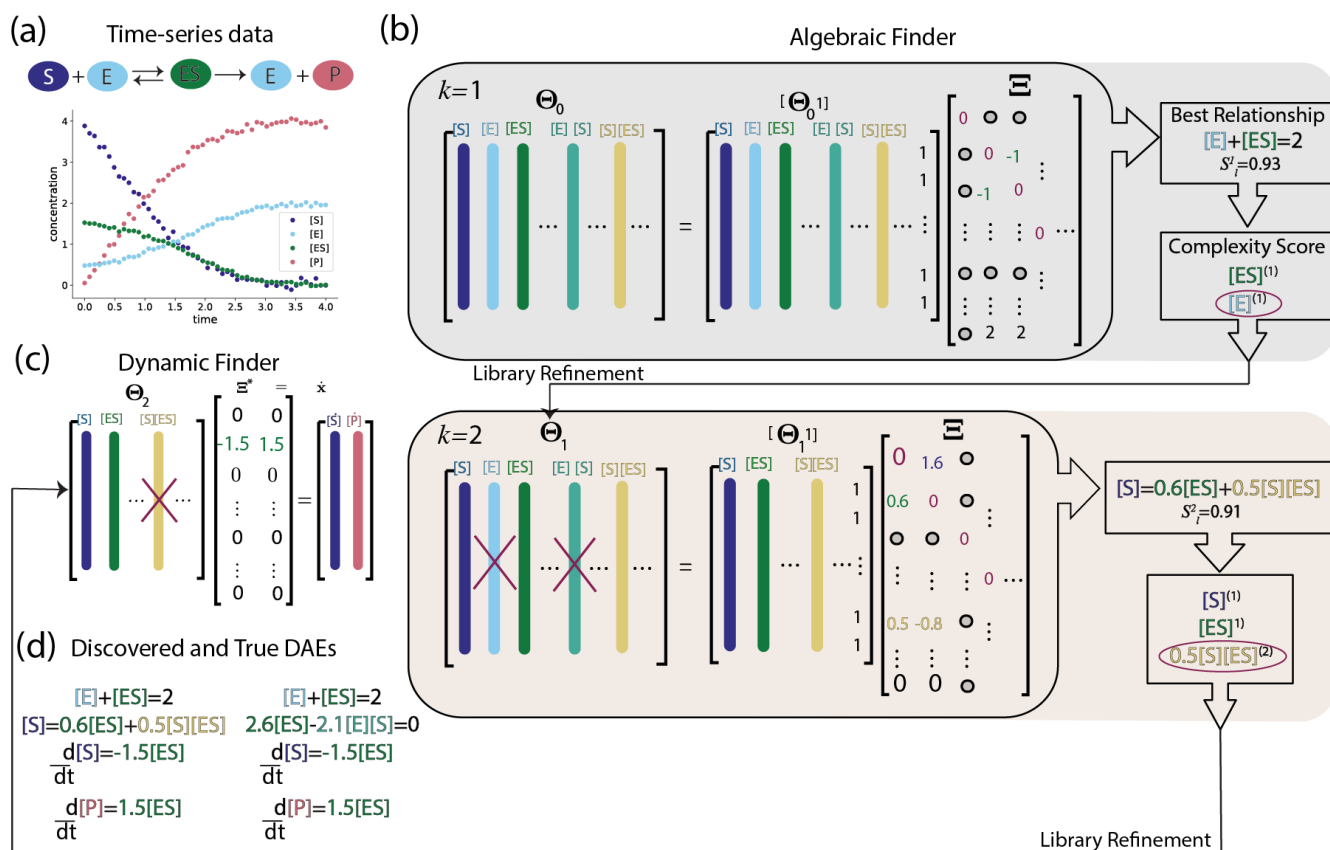


Figure 1. SODAs algorithm explained using a chemical reaction network example. (a) Collect time series and construct candidate library matrix. (b) Algebraic Relation Finder: iteratively finds algebraic relationships and refines the candidate library based on the discovered relationship. In each iteration k , the best relationship is selected based on its score S^k , and a complexity score is assigned to each term within this relationship. This complexity score is used to select a term to refine the candidate library for the next iteration. (c) Dynamic Finder: the refined candidate library from the algebraic finder step is used to find the system of ODEs. (d) Assembled DAEs: The algebraic and differential equations from the algebraic and dynamic finder steps respectively, are assembled to form the final set of DAEs (left), which is equivalent to the true set of DAEs (right).

in equations (2)–(3) can be written as linear combination of a set of predefined library terms which comes from prior knowledge. We start by defining a candidate library $\Theta = \{\theta_1(\mathbf{x}), \dots, \theta_J(\mathbf{x})\}$, which is a set of functions of the state variables. Based on the time-series data \mathbf{X} , we next form the initial candidate library matrix denoted by $\Theta_0 = [\theta_1(\mathbf{X}) \ \theta_2(\mathbf{X}) \ \dots \ \theta_J(\mathbf{X})]$, which is an $N \times J$ matrix where the j^{th} column represents the evaluation of the candidate function θ_j at time points $\{t_1 = 0, \dots, t_N = T\}$. The DaeFinder package provides various choices for library functions and their corresponding matrix creation, such as polynomial monomial libraries, Fourier series, phase-difference terms, and various custom functions that can be controlled using a connectivity matrix (which is useful in applications like power-grid networks where pre-existing knowledge about connections between nodes can guide library construction). We have also developed the package to interface with the PySINDy package [42] such that PySINDy’s library construction features can also be used with DaeFinder. In our applications, a polynomial library is used for the CRN and the nonlinear pendulum, while a combination of polynomial and trigonometric functions is used for the power grid. After forming the candidate library, SODAs consists of two major steps: the algebraic finder step (Figure 1b) and the dynamical system finder step (Figure 1c).

Identifying algebraic relationships through iterative sparse optimization

For many systems, it is unclear *a priori* which states are differential variables and which are algebraic, especially if separation of timescales is expected and a subset of variables are in quasi-steady state. Our approach does not necessarily require pre-existing knowledge about which states are in the algebraic relations. Notwithstanding, prior knowledge on state variables that take part in algebraic equations can be incorporated into the pipeline. For unknown algebraic equations, the algebraic finder step involves iteratively identifying algebraic relationships and reducing multicollinearity in the library by removing these relationships.

Once all algebraic equations are found, the remaining dynamical equations are identified from the refined library using an existing method like SINDy [10, 16, 18] or IDENT [29, 30].

At each k^{th} iteration of the algebraic finding step, we start with a refined candidate library matrix Θ_{k-1} , where Θ_0 represents the initial candidate library matrix Θ (Figure 1b). Let \mathcal{J}_k represent the index set for elements of Θ_k and $J_k = |\mathcal{J}_k|$. Assuming no prior information about the number of algebraic relationships and which state variable functions are part of algebraic relationships, we sparsely fit each member of the candidate library Θ_{k-1} against the rest of the library. That is,

$$\theta_l(\mathbf{x}) = \sum_{\substack{j \in \mathcal{J}_k \\ j \neq l}} p_j^l \theta_j(\mathbf{x}), \quad l \in \mathcal{J}_{k-1}. \quad (12)$$

To enforce sparsity, such that most of the regression parameters $p_j^l = 0$ for $j \in \mathcal{J}_{k-1}$, the following loss function can be minimized:

$$L_l(\mathbf{p}^l) = \sum_{r=1}^N \left\| \theta_l(\mathbf{x}(t_r)) - \sum_{\substack{j \in \mathcal{J}_k \\ j \neq l}} p_j^l \theta_j(\mathbf{x}(t_r)) \right\|^2 + \alpha \|\mathbf{p}^l\|_0, \quad l \in \mathcal{J}_{k-1}. \quad (13)$$

In matrix form, this series of regression problems can be written as

$$\Theta_{k-1} = \Theta_{k-1} \Xi, \quad (14)$$

where $\Xi = [\mathbf{p}^1 \ \mathbf{p}^2 \ \dots \ \mathbf{p}^{J_k}]$ with constraints $\Xi_{jj} = 0$ and $\|\Xi\|_0$ is minimized (Figure 1b, *left*). Note that, in practice, the matrix form is not used, but instead each \mathbf{p}^l is optimized in parallel by minimizing the loss function $L_l(\mathbf{p}^l)$. A similar parallelized approach is introduced in [27] for semi-combinatorial discovery of implicit equations of the form (11), whereas in SODAs this parallel fitting approach is used for finding algebraic relationships. Notably, derivatives are not involved in the algebraic finder step and do not need to be estimated from the noisy data. There are multiple established approaches to enforce the sparsity of the parameter matrix Ξ . The `DaeFinder` package supports popular alternatives to ℓ_0 regularization, including LASSO and various sequential-thresholding methods combined with regularizers like Ridge regression and Elastic Net. Previous work has shown that soft thresholded ordinary least squares estimator (STOLS) outperforms the usage of LASSO alone for SINDy [43]. Accordingly, we employed LASSO followed by sequential thresholding as the default solver in our numerical experiments, unless specified otherwise.

Improving numerical conditioning of the candidate library

The next step of the algorithm is to select the best-fitting algebraic relationship across all the candidate fits in (13) (Figure 1b, *right*). To identify the most likely relationship, we assign a score S_l^k to each candidate fit in (13). In our examples, we have used the coefficient of determination \mathcal{R}^2 [44], which ranges from 0 to 1, where larger values indicate a good fitting. Other criteria, such as AIC and BIC (see [45, 46]), that balance training error with model simplicity can also be used to define S_l^k . The fit with the highest score is then identified as the most prominent algebraic relationship in the library Θ_{k-1} and is further used to refine Θ_{k-1} . In our experience, conservation laws that involve first-order terms are initially identified as the best relationships during this process.

After identifying the best algebraic relationship based on the score S_l^k for the k^{th} iteration, any common factors in that relationship are factored out to obtain a reduced equation $g_k(\mathbf{x}) = 0$. To address the multicollinearity introduced by this algebraic relationship, we remove one of the terms in $g_k(\mathbf{x})$. To decide which term to remove, each term $\theta^{(k)}$ in $g_k(\mathbf{x})$ is assigned a complexity score (Figure 1b, *right*). In polynomial libraries, this score is set to be the degree of the term by default, i.e., higher-degree monomials should have a higher complexity score. The term with the highest complexity score, $\theta_{\text{high}}^{(k)}$ (circled in Figure 1b, *right*), is then removed from the library. The rationale behind this refinement is that if $\theta_{\text{high}}^{(k)}$ is part of the discovered algebraic relationship $g_k(\mathbf{x}) = 0$, then $\theta_{\text{high}}^{(k)}$ can be expressed as a linear combination of the other terms in $g_k(\mathbf{x})$, so there is no loss of information by removing a term from the library. By keeping lower rather than higher complexity terms in the library, we reduce noise amplification [47]. If multiple terms share the same complexity score, then either expert knowledge or quality of measurement of states (through statistical measures like variance) can also be used to choose one term over the other, or a term can be selected randomly. Additionally, for any $\theta \in \Theta_{k-1}$, the equation $\theta g_k(\mathbf{x}) = 0$ also represents a potential algebraic relationship that can lead to perfect multicollinearity. To remove all degenerate relationships of the form $\theta g_k(\mathbf{x}) = 0$, all multiples of $\theta_{\text{high}}^{(k)}$ are also removed from Θ_{k-1} . Let Γ_k be a subset of the candidate library matrix Θ_{k-1} that has $\theta_{\text{high}}^{(k)}$ as a factor; then $\Theta_k = \Theta_{k-1} \setminus \Gamma_k$, where all elements of Γ_k are removed from Θ_{k-1} as part of the refinement process. It follows that the libraries at each refinement step form a decreasing chain, $\Theta_k \subset \Theta_{k-1} \subset \dots \subset \Theta_0$.

Mitigating perfect multicollinearity in the candidate library

As an example, in the CRNs (4)–(7), the algebraic relationship $[E] + [ES] - E_0 = 0$ can cause the following perfect multicollinearity in the candidate library matrix Θ that has up to degree 2 monomials:

$$[E] + [ES] - E_0 = 0, \quad (15)$$

$$[E]([E] + [ES] - E_0) = 0, \quad (16)$$

$$[S]([E] + [ES] - E_0) = 0, \quad (17)$$

$$[P]([E] + [ES] - E_0) = 0, \quad (18)$$

$$[ES]([E] + [ES] - E_0) = 0. \quad (19)$$

For higher-order candidate libraries, there will be more relationships. All such degenerate algebraic relationships make up the nullspace of the library matrix Θ . If any one of the degenerate equations (16)–(19) is identified as the relationship with the best S_I^k , it is first reduced to the form (15). Both terms in this reduced relationship (i.e., $[E]$ and $[ES]$) have the same complexity score of 1 based on the degree of the monomial (Figure 1b, *top-right*). In the absence of any other information, we randomly choose to select $[E]$ to refine the library. Consequently, all factors of $[E]$ including $[E]$, $[S][E]$, $[P][E]$, $[ES][E]$, and $[E]^2$ are removed from the candidate library Θ_0 (see how Θ_1 is defined for $k = 2$ in Figure 1b). This process of algebraic equation discovery and library refinement are iteratively continued until all algebraic relationships are discovered. Note that the algebraic equations found will not be unique because any linear combination of algebraic equations can lead to another algebraic relationship, but our approach tries to find a minimal set of equivalent algebraic relationships that can form any algebraic relationship using linear combinations.

For many applications, such as power-grid networks, the number of algebraic constraints in a DAE system is known beforehand from physical principles such as the conservation of energy at each node. However, for other applications, such as CRNs, the number of algebraic constraints is not known in advance. When the number is unknown, an SVD analysis of the candidate library matrix Θ_{k-1} can be used to track the number of algebraic relationships remaining in the library (Figure 2) at iteration k . The right singular vectors (principal components) with zero singular values correspond to linear combinations in the library with zero variance (i.e., perfect multicollinearity), so the nullity of the covariance matrix estimates the number of algebraic relationships. The variance-explained ratio calculated for each singular value captures the relative importance of each principal direction in the library more clearly than the raw singular values. The ratio is the variance explained by each principal direction or singular value squared normalized by the total variance of the library or, equivalently, the sum of all singular values. When noise levels are minimal, there is a clear separation between the singular vectors lying in the nullspace and the dominant principal components. As the library is refined based on valid algebraic relationships, the zero singular values disappear while the number of dominant principal components remains constant until all zero singular values are removed (Figure 2a).

Even at high noise, where the separation becomes less clear, the SVD spectrum can indicate whether the refinement is based on a true algebraic relationship in the library. For instance, at 15% noise in Figure 2b, refining the library using the term $[E]$ (which is part of an algebraic relationship) reduces the number of zero singular values while keeping the number of dominant principal directions—those with relatively large variance explained—unchanged. In contrast, refining it using $[P]$ (which is not part of any algebraic relationship) causes a loss in the number of dominant principal directions. Through a correct refinement, the candidate library can become significantly smaller and better-conditioned, aiding the discovery of dynamic equations. The effect of a series of correct library refinements in removing only low-variance-explained-ratio values is more pronounced for libraries with higher-order terms (e.g., monomials up to degree 4, see Figure 2c). If the number of algebraic relationships K in the DAE system is not known beforehand, it can be treated either as a hyperparameter or determined via a Pareto front analysis of the library's condition number improvements, which can serve as a stopping criterion for the algebraic discovery and refinement process i.e., $\text{Cond}(\Theta_{K+1}) \approx \text{Cond}(\Theta_K) < \text{Cond}(\Theta_{K-1}) < \dots < \text{Cond}(\Theta_0)$. By default, we use lack of improvement in condition number to determine K . For example, the improvement in conditioning stagnates after the first two refinements for the CRN example, and so the Pareto front suggests stopping library refinement after the second equation is removed (Figure 2d).

In the `DaeFinder` package, the `AlgModelFinder` class provides many features to automate the steps in the algebraic finding step. This class supports various metrics for assigning scores to different algebraic relationships discovered as part of (13), including \mathcal{R}^2 values, mean squared error on test sets, etc. It also has functions to reduce the algebraic relationships and refine the candidate library based on SODAs.

Identifying differential variables and their differential equations

Once the algebraic relations are found, the differential equations remain to be discovered. However, we must first assign which state variables will be treated as differential variables. Each algebraic relationship will impose algebraic constraints on one or more of the state variables. If multiple variables are part of an algebraic relationship, domain expertise or quality of

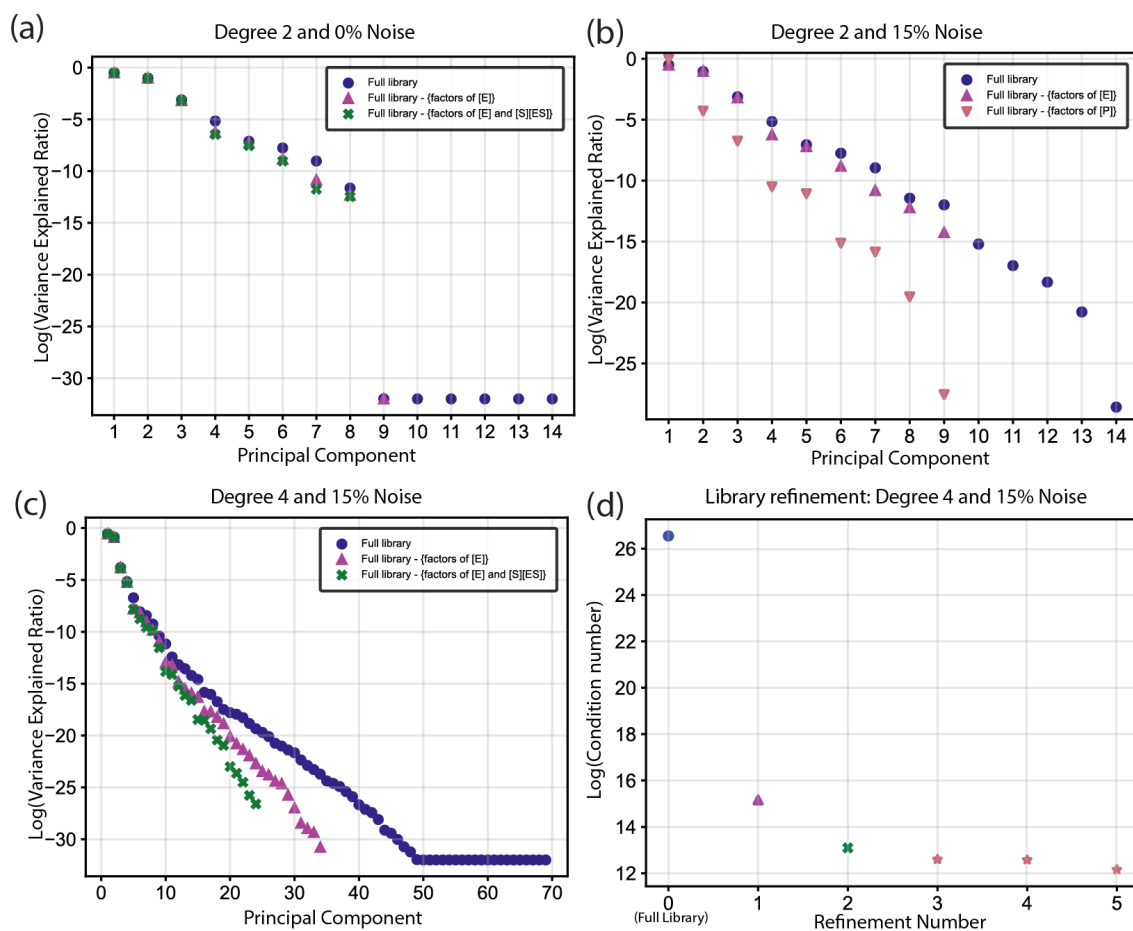


Figure 2. SVD analysis of the candidate library Θ : (a) library with monomials up to degree 2 and no noise, (b) library with monomials up to degree 2 and 15% noise, (c) library with monomials up to degree 4 and 15% noise, (d) tracking condition number after each refinement for library with monomials up to degree 4 and 15% noise. SVD analysis helps track redundancies in the candidate library space and determines when to stop iterations in the algebraic finder step.

measurements can be used to decide which variables should be identified as the differential variables in the DAEs. For example, the concentration of enzyme complexes in a CRN are often selected as the algebraic variables because they are difficult to measure directly, and it is advantageous to reduce them out of the system through substitution of the algebraic equations as in (9). Therefore, metabolite concentrations may be preferred as the differential variables. Another consideration is the quality of measurements and the ability to find accurate time derivatives of state variables. If a state variable exhibits a relatively high dynamic range in measurement and we have access to high-quality, high-sampling measurements of this state, then this state can be treated as a differential variable.

For the identified differential variables, any existing methods for ODE discovery (e.g., SINDy) can be used to find the dynamics equations in the DAE system (Figure 1c). This is the stage where noisy derivatives affect recovery, and there are various approaches to mitigate noise, including weak formulation approaches [16–18] and smoothing functions [14, 48]. Currently, `DaeFinder` package supports finding derivatives using finite difference methods and using smoothing filters like splines and Savitzky-Golay filters [48]. The latter is used in our examples. For numerical experiments, we have used LASSO followed by sequential thresholding to solve the sparse optimization. Finally, we obtain a set of differential and algebraic equations of the form (2)–(3) (Figure 1d).

4 Results

We demonstrate the capability of SODAs to discover DAEs and identify reduced coordinate systems through three distinct examples. In Example 1, SODAs rediscovers the underlying DAEs of CRNs with varying complexity, demonstrating the identification of conservation laws and quasi-steady states. Example 2 applies SODAs to pixel data from real-time experiments

Algorithm 1: SODAs: Sparse Optimization for Differential-Algebraic Systems

Input: \mathbf{X} , K , Θ , α , `sparse_fit`, `score_function`

Output: discovered DAEs

Step 1: Construct library matrix:

$\Theta_0 = [\theta_1(\mathbf{X}), \dots, \theta_j(\mathbf{X})]$

Step 2: Algebraic Finder

$k = 1$ *%set iteration index*

`condition_number_improved` = True *%flag to check if condition number of library has improved.*

while ($k \leq K$ or `condition_number_improved`) **do**

foreach $\theta_l \in \Theta_{k-1}$ (*done in parallel*) **do**

`sparse_fit`(Θ_{k-1}, α) *%solve sparse regression problem $\theta_l(\mathbf{x}) = \sum_{\substack{j \in \mathcal{J}_k \\ j \neq l}} p_j^l \theta_j(\mathbf{x}) + \alpha \|\mathbf{p}^l\|_0$.*

$S_l^k = \text{score_function}(\mathbf{p}^l, \Theta_{k-1})$

Library Refinement Steps:

$m = \arg \max(S_l^k)$ *%find the best relationship based on the maximum score.*

$g_k(\mathbf{x}) = \text{equation_reduce}(m, \Theta_{k-1})$ *%reduce the equation $\theta_m(\mathbf{x}) = \sum_j p_j^m \theta_j(\mathbf{x})$ to $g_k(\mathbf{x}) = 0$.*

$\theta_{\text{high}}^{(k)} = \text{select_term}(g_k(\mathbf{x}))$ *%select the term inside $g_k(\mathbf{x})$ based on the highest complexity ranking.*

$\Gamma_k = \text{factors}(\theta_{\text{high}}^{(k)}, \Theta_{k-1})$ *%identify all factors of $\theta^{(k)}$ in Θ_{k-1} .*

$\Theta_k = \Theta_{k-1} \setminus \Gamma_k$ *%update the library.*

`condition_number_improved` = `bool`(`Cond`(Θ_k) – `Cond`(Θ_{k-1}) < ϵ_k)

$k = k + 1$

$\Theta_* = \Theta_{k-2}$ *%final refined library.*

Step 3: Dynamical System Finder

$\mathbf{y} = \text{find_dynamic_states}(\mathbf{x}, \{g_k\}_{k=1}^K)$ *%finding dynamic states based on discovered algebraic equations.*

$\mathbf{F}(\dot{\mathbf{y}}, \dot{\mathbf{y}}, \mathbf{x}, \dots) = 0 \leftarrow \text{discover_ODEs}(\mathbf{y}, \Theta_*)$ *%discovering ODEs using refined library.*

return $\{\{g_k\}_{k=1}^K\}, \mathbf{F}$ *%return discovered DAE system.*

Inputs and Parameters:

- \mathbf{X} : Data matrix $\mathbf{X} \in \mathbb{R}^{N \times d}$ (time-series data).
 - K : Number of previously known algebraic relationships in the library. Default: $K = \text{None}$.
 - Θ : Class of candidate library functions. `DaeFinder` package supports monomials of varying degrees, trigonometric functions, phase difference terms for power grid, etc.
 - α : Regularization parameter for the sparse regression. Default: $\alpha = 0.2$.
 - `sparse_fit`: Function to perform sparse regression, e.g., LASSO, STOLS, etc. Default: LASSO followed by sequential thresholding.
 - `score_function`: Function to evaluate the quality of sparse fitting. Choices include \mathcal{R}^2 , AIC, BIC, etc. Default: \mathcal{R}^2 .
 - `equation_reduce`: Function to simplify the best algebraic relationship by taking out common factors in the equation.
 - `select_term`: Select the highest-ranked term in the reduced equation based on some predefined complexity criteria. Default: for monomial candidate library, degree is used to define rank.
 - `factors`: Identifies the factors of the selected term inside the library.
 - ϵ_k : Tolerance used for stopping the refinement. In practice, this is found using a Pareto front tracking the improvement in `Cond`(Θ_k).
 - `find_dynamic_states`: Function to choose dynamic states out of the state space. Various criteria are discussed in Section 3.
 - `discover_ODEs`: Function representing any suitable algorithm to discover differential equations. `DaeFinder` currently supports the strong form of SINDy with smoothening splines [10, 14] and Savitzky-Golay smoothing filters [48].
-

or animated video of three different cases of nonlinear pendulum: a singular pendulum with negligible damping, a heavily damped pendulum, and a chaotic double pendulum. This example shows SODAs can discover the algebraic constraints and the corresponding reduced coordinate system when such relations are not readily apparent from pixel data. In Example 3, SODAs rediscover DAEs used in power-grid modeling for three benchmarks (IEEE-4, IEEE-9, and IEEE-39) demonstrating recovery of network topology when the library contains trigonometric functions.

In Examples 1 and 3, where the time series were generated synthetically, we assess data requirements, robustness to noise, and sensitivity to different types of perturbations are studied. For a simulated time-series states, \mathbf{X}_i , Gaussian noise is sampled and added to the time series as

$$\mathbf{X}_{i,\text{noisy}} = \mathbf{X}_i + \text{noise}\% \cdot \sigma_i \cdot \mathcal{N}(0, 1), \quad (20)$$

where $\text{noise}\%$ is the percentage of noise, $\sigma_i = \text{std}(\mathbf{X}_i)$, and $\mathcal{N}(0, 1)$ is the standard normal random variable. In Example 2, the pixel data was extracted from video footage, which inherently introduced noise into the dataset. In Examples 1 and 2, we explore the impact of polynomial library size on data requirements.

4.1 Example 1: Chemical Reaction Networks

We demonstrate the ability of SODAs to accurately recover governing equations from simulated time series of known CRNs, even as system complexity and extrinsic noise increase. In applications in chemistry and biology, the temporal evolution of each chemical species in a CRN can be modeled using mass-action kinetics [49, 50]. This naturally leads to models consisting of polynomial terms of concentration of chemical species. However, timescale separations in the equilibration rates of different species motivate quasi-steady-state approximations [36, 51] which simplify mathematical analysis by reducing the state space dimension while accounting for important interactions and temporal features [52].

Using SODAs to rediscover the governing equations of CRNs is motivated by unifying the common task of model reduction in chemical and biological networks with model discovery. For known models, a wealth of techniques exist to simplify model representation and reduce complexity. Without loss of information, models can be simplified through conservation analysis, partitioned into sub-networks, or non-dimensionalized. Beyond quasi-steady-state approximations, other reduction techniques include methods that exploit optimization and sensitivity analysis [53]. Although model reduction concepts have previously been associated with neural network-based model discovery [54, 55], SODAs demonstrates these concepts clearly within the framework of regression-based sparse-model selection, leveraging conservation analysis and relevant timescale for interpretable reduction when the model structure is unknown.

In this example, we use time series generated from three CRNs of varying complexity consisting of one, two, and four enzyme-mediated reactions (Figure 3a). The four-reaction system describes the simplified propanediol utilization pathway native to *Salmonella enterica* [56, 57]. Details of pathway simulation are included in supplementary Section 1.1. Our data-driven discovery of the pathway at noise levels realistic to those present in metabolite measurement [58, 59] shows the utility of SODAs in detecting the relevant system timescales and offers a guideline on its data requirements and noise robustness.

System description

As introduced in the example in Section 2.2, CRNs for the concentrations $\mathbf{x} = [\mathbf{M}]$ of species $\mathbf{M} = [M_1, M_2, \dots, M_N]^\top$ describe reactions between species as



where α_{ij} , β_{ij} denote the reaction's chemical coefficients and k_{ij} the reaction's rate constant. For example, a reaction that converts one unit of M_1 to one unit of M_2 at rate k_1 is written as $\alpha_{1,1} M_1 \xrightarrow{k_1} \beta_{2,1} M_2$, where $\alpha_{1,1} = \beta_{2,1} = 1$. A CRN model with d reactions can therefore be expressed in matrix form as

$$\frac{d\mathbf{x}}{dt} = \mathbf{S}\mathbf{v}(\mathbf{x}) \quad (22)$$

where $\mathbf{v}(\mathbf{x}) = [v_1(\mathbf{x}), v_2(\mathbf{x}), \dots, v_d(\mathbf{x})]^\top$ is the reaction rate vector with entries defined as $v_j(\mathbf{x}) = k_j \prod_{i=1}^N x_i^{\alpha_{ij}}$. The stoichiometry matrix $\mathbf{S} \in \mathbb{R}^{N \times d}$ encodes the connectivity of the reactions between species according to the net production $S_{ij} = \beta_{ij} - \alpha_{ij}$ of species i through reaction j for each reaction $j = 1, \dots, d$. For instance, the reaction $M_1 \xrightarrow{k_1} M_2$ leads to the stoichiometry matrix $\mathbf{S} = [-1, 1]^\top$. Thus, reactions comprising a single species will be linear, but those involving two or more species will be nonlinear.

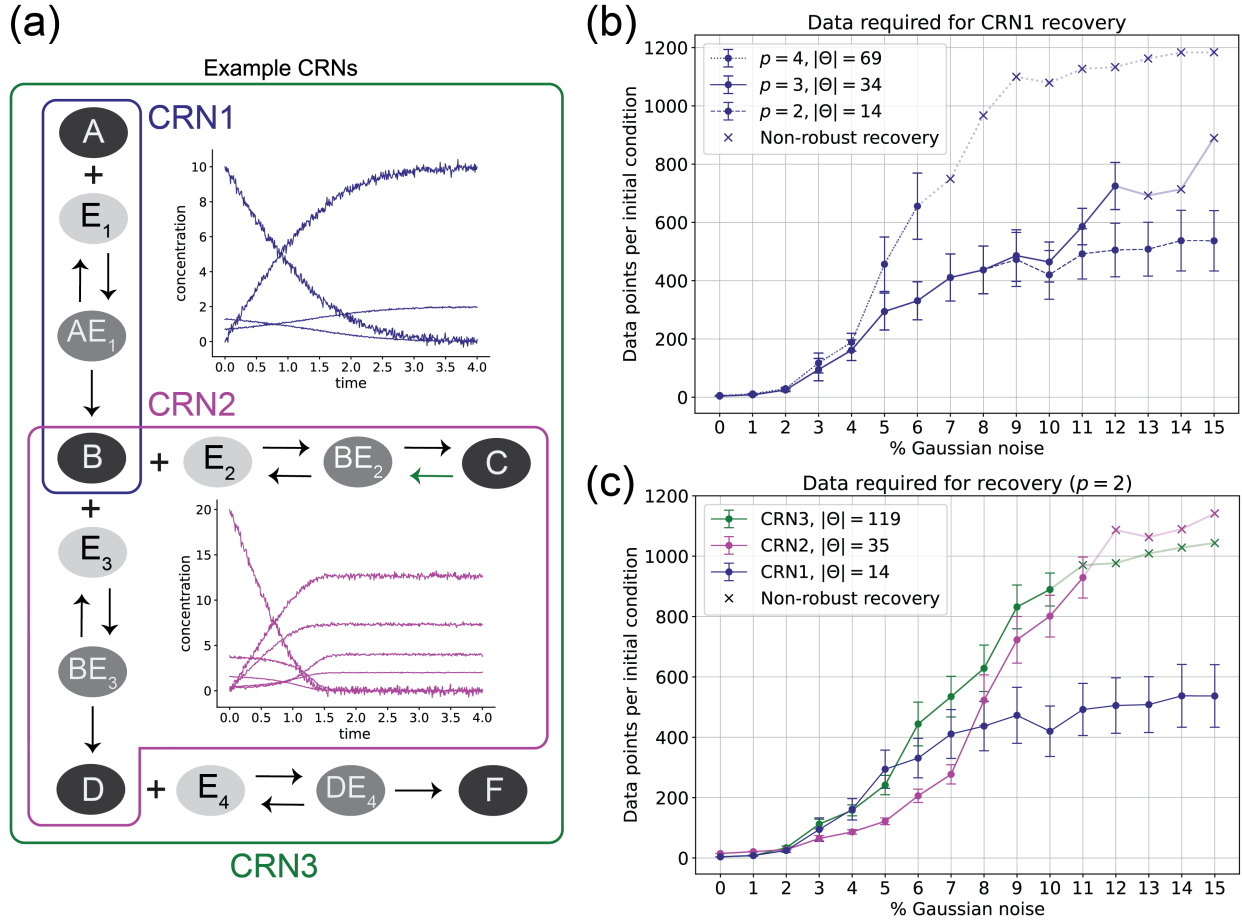


Figure 3. Example 1: Application to chemical reaction networks. (a) Nested structure of CRN1 and CRN2 within CRN3 and examples of simulated time-series with 5% noise. Note that only CRN3 allows reversibility of $C \rightarrow BE_2$ as denoted by the green arrow. (b) Scaling of the data required for recovery of the correct algebraic equations in CRN1 across library degree p and cardinality $|\Theta|$. Non-robust recovery is denoted when fewer than 80% of random seeds succeeded in recovering the correct algebraic relationships. Error bars represent standard error across 10 random noise seeds. (c) Scaling of the data required for recovery of the correct algebraic equations for all CRNs (cardinalities noted) with fixed library degree $p = 2$.

Algebraic relationships arise in CRNs in two ways. First, the conservation of mass between multiple species considered in the CRN (e.g., enzyme and enzyme-substrate complex) leads to a first-order algebraic relationship (e.g., (17)). Second, a quasi-steady-state approximation resulting from time-scale separation partitions \mathbf{x} into "fast species" \mathbf{y} and "slow species" \mathbf{z} , so $\mathbf{x} = [\mathbf{y}, \mathbf{z}]^T$ with approximation $\frac{d\mathbf{y}}{dt} = 0$. This results in a set of algebraic relationships given by the solutions of

$$\mathbf{S}_y \mathbf{v}(\mathbf{y}, \mathbf{z}) = 0 \quad (23)$$

where \mathbf{S}_y is the submatrix containing only the reactions involving \mathbf{y} . Within the SODAs framework, the goal is to identify the DAE with algebraic equations $\mathbf{G} = \mathbf{S}_y \mathbf{v} = 0$ and dynamic equations $\mathbf{F} = \frac{d\mathbf{z}}{dt} = \mathbf{S}_z \mathbf{v}$, where \mathbf{S}_z contains only the reactions involving \mathbf{z} . Substitution of algebraic relationships via the implicit definition of \mathbf{y} in terms of \mathbf{z} allows for the expression of the system entirely in terms of \mathbf{z} . With $\mathbf{y} = \mathbf{g}(\mathbf{z})$, CRN dynamics are given by

$$\frac{d\mathbf{x}}{dt} = \frac{d\mathbf{z}}{dt} = \mathbf{S}_z \mathbf{v}(\mathbf{g}(\mathbf{z}), \mathbf{z}). \quad (24)$$

As all terms in the non-reduced model are polynomial, the reduced model takes the rational form in (10). This form was the target of discovery by implicit-SINDy [26] and PI-SINDy [27]. An advantage of discovering the DAE form rather than the related rational equations is that we discover which variables are in quasi-steady state rather than assuming that all measured variables are inherently dynamic. Note that this means that SODAs requires measurements of both algebraic and differential

variables, which is unlikely for realistically-sized biological or chemical networks. Future work to lessen the burden of unobserved states is discussed in Section 5. In realistic examples, the method in its current form may be best-suited instead for model reduction during the simulation of large CRNs, which is an ongoing area of study [60,61]. For definitions of \mathbf{S}_z and \mathbf{v} in all tested CRNs, see supplementary Section 2.1.

SODAs application.

We start with the discovery of the equations of CRN1, the single irreversible Michaelis-Menten reaction. Within the seemingly simple dynamics, there exist three distinct algebraic relationships, two induced by mass conservation and one by separating the state variables \mathbf{x} as $\mathbf{x} = [\mathbf{y}, \mathbf{z}]^\top$, resulting in a system of the form in (23)-(24). Of the two mass conservation relationships, one is of the form (15) (i.e., conservation of enzyme) and the other relates $[A]$ and $[B]$ with a constant M^{tot} representing total non-enzyme mass (i.e., conservation of substrate). The single algebraic relationship emerging from the quasi-steady-state approximation takes the implicit form of

$$[AE_1] = \frac{(E_1^{\text{tot}} - [AE_1])[A]}{K_{M1} + [A]} \quad (25)$$

where K_{MN} is the Michaelis constant for reaction N derived from the set $\{k\}$ of the reaction's rate constants from (21). Expanding the above implies an algebraic relationship between terms $[AE_1]$, $[AE_1][A]$, and $[A]$ as in (19).

To discover such relationships from our simulated time series, we first constructed a candidate library using a monomial basis of degree p in states \mathbf{x} . Such a basis allows for the discovery of two of the three algebraic relationships when multiple simulations of the CRN are used. Because M^{tot} varied between simulations, identification of the substrate conservation relationship was not possible in our setup, as a single learned M^{tot} cannot fit all simulations. This was not the case for the enzyme conservation relationship, as E_{tot} was held constant between simulations. Inclusion of non-zero initial conditions in Θ would allow for the discovery of substrate conservation, a close analog to the inclusion of suspected bifurcation parameters in Θ in the original formulation of SINDy [10] and following work. We chose here to exclude initial conditions from Θ because when any two (or more) initial conditions are held constant across simulations, they will be in perfect correlation, confounding one another and limiting the identifiability and interpretability of any resulting algebraic relationships. Because substrate mass conservation can be checked by simply observing whether the system is open or closed, we deemed it reasonable that this third algebraic relationship does not benefit from sparse regression for its discovery. If this is not a reasonable assumption, for example in a large or particularly complex system, note that simulations or experiments may be designed alternatively such that initial conditions in Θ do not have these colinearities (see Section 5).

We performed discovery for CRN1 using degree $p = 2, 3, 4$ libraries with a range of 0-15% noise to assess the data requirements for successful recovery of algebraic relationships with SODAs (Figure 3b). In the context of CRNs, this gives a reference for the quality and resolution of data needed to determine whether mass is conserved among a subset of states or if there is timescale separation in certain reactions sufficient for quasi-steady-state approximations to hold. For each application of SODAs, data was preprocessed using Savitzky-Golay filters [48] to smooth noisy derivatives. We used the results of the Pareto front approach referenced in Section 3 to determine that the library should be refined two times. Since we were interested not simply in the minimum data to achieve rediscovery of the correct algebraic equations, but the minimum data to ensure rediscovery at a given resolution and any resolution finer, we defined the SODAs data requirement to be the number of uniformly spaced data points per initial condition above which algebraic relationship recovery was ensured up to a tested maximum of 1200 data points per initial condition. Note that this does not prevent time series with lower data resolution than those indicated in Figure 3b from being used for successful model discovery with SODAs. In low-resolution cases, the impact of noise on the regression problem is heightened, meaning that correct discovery may be possible but is dependent on the particular realization of measurement error (see supplementary Section 2.2). Subsequent discovery of the dynamic equations returned the correct structure and parameter sufficiently similar to those used for simulation (see supplementary Section 2.4 for parameter fitting results at varied noise).

All algebraic relationships were correctly recovered with up to 15% noise for all degrees of p tested. Even for large magnitudes of noise, SODAs required a lower resolution and far fewer sampled initial conditions for recovery than implicit-SINDy [26] or PI-SINDy [27]. The amount of data required for recovery across library degrees scaled similarly for low noise, but the introduction of higher-order terms in the $p = 3$ and $p = 4$ libraries lead to a sharp increase in the data requirement as noise becomes significant. Due to corruption of the signal and noise amplification, these higher-order terms induce spurious algebraic relationships with correlations similar to those of true relationships for low time-series resolutions. For both $p = 3$ and $p = 4$, as the noise was increased beyond 12% and 6% respectively, recovery failed to be robust. This suggests that there are certain noise realizations for which ≤ 1200 data points are sufficient for rediscovery, but it should not be expected.

Testing recovery in the more complex CRN2 and CRN3 examples demonstrates how SODAs responds to a larger state space, richer dynamics, and, as a consequence, more complex algebraic relationships. In the tested CRNs of higher dimension,

the same type of relationships exist as in CRN1: each enzyme is conserved, and each reaction equilibrates in a manner that makes a quasi-steady-state approximation reasonable. However, because of coupling between the reactions, these algebraic relationships can appear with an increased complexity and number of terms, where it is not immediately obvious the exact physical property from which they result. Take, for example, the quasi-steady-state approximations made in CRN2 (Figure 3a). Quasi-steady-state approximations for both the $B \rightarrow C$ and $B \rightarrow D$ reactions mediated by enzymes E_2 and E_3 respectively, give the implicit relationships

$$[BE_2] = \frac{(E_2^{\text{tot}} - [BE_2])[B]}{K_{M2} + [B]} \quad [BE_3] = \frac{(E_3^{\text{tot}} - [BE_3])[B]}{K_{M3} + [B]} \quad (26)$$

in the same form as (25) once we assume that $[E_2]$ and $[E_3]$ have been removed from the library by a previous iteration of SODAs due to mass conservation. Note that the choice to remove enzymatic terms instead of their complexes is a standard choice to derive the Michaelis-Menten dynamics [37, 38], but either the enzyme or the complex could be removed according to the SODA algorithm, as they are of equal order. Isolating $[B]$ in each expression in (26), we equate to find

$$2(K_{M3} - K_{M2})[BE_2][BE_3] = K_{M3}E_2^{\text{tot}}[BE_3] - K_{M2}E_3^{\text{tot}}[BE_2] \quad (27)$$

which suggests that the quasi-steady-state approximation relationships should ultimately appear in the candidate library as an algebraic relationship in terms of $[BE_2][BE_3]$, $[BE_3]$, and $[BE_2]$. An analogous derivation exists for CRN3.

In each application of SODAs, Savitzky-Golay filters were again applied [48] to smooth noisy derivatives. For CRN2, Pareto front analysis correctly suggested three refinements, while, for CRN3, it correctly suggested five (see supplementary Section 2.3). We again assessed the response of the method to increasingly noisy data across a variety of resolutions at fixed polynomial degree $p = 2$ (Figure 3c). While we find a similar scaling of the data requirement with respect to noise as in Figure 3b, there is a notable difference in how the data requirement responds to an increase in underlying model complexity vs. an increase in library degree, even if the two modifications lead to Θ of similar cardinality. For example, $p = 2$ recovery for CRN2 requires significantly more data points per initial condition than $p = 3$ recovery for CRN1 at $> 8\%$ noise, despite the two cases having $|\Theta| = 35$ and $|\Theta| = 34$, respectively. From this we may hypothesize that SODAs performance is more sensitive to the library degree than the dimension of the library's monomial basis, a notion consistent with our earlier discussions on the impact of higher-order terms on library correlation. Our results also showed that it is not necessarily the case that more complex underlying models always have higher data requirements for rediscovery, as there were regimes where CRN2 required fewer data points per initial condition than CRN1, and regimes where CRN3 required less data than CRN2 despite both requiring more than CRN1. This points towards the importance of data sampling; simply the quantity of the data alone does not determine its ability to inform sparse-model selection, and, for example, the types of dynamics sampled within the data may be important to model discovery.

4.2 Example 2: Non-linear and Chaotic Pendulums

In this example, we demonstrate the capability of SODAs to identify a reduced coordinate system from pixel data obtained from video footage of two different types of pendulums across three different scenarios: 1) real-time footage of a single pendulum exhibiting non-linear behavior through large-angle swings, 2) video recordings of the animation of a highly damped pendulum, and 3) video recordings of the animation of a double pendulum exhibiting chaotic behavior. Screen recordings of the animation were used for 2 and 3 to mimic the process of extracting data from video, even though a simulation was used to produce the animation. These cases illustrate the use of SODAs in mechanical systems, where state measurements are obtained through images, videos, or sensor data.

When modeling the motion of mechanical systems, there often exist coordinate transformations that lead to simple equations explaining the motion. For example, the natural coordinate system for modeling the motion of a single pendulum is known to be the one-dimensional polar coordinate system, i.e., to model the angle ω that the pendulum makes with a reference axis in the 2D plane (Figure 4a - top) or in the case of a double pendulum, the two angles, ω_1, ω_2 , that the two pendulums make with the reference axis (Figure 4a - bottom). However, finding the appropriate coordinate transformation to produce the most parsimonious system is often challenging and not clear from raw measurements of the states. Recently, several data-driven methods have been used to find reduced coordinates, for example, using neural networks to learn nonlinear mappings to a lower-dimensional state-space [62, 63]. Here, we show how SODAs can assist in this process using the algebraic finder step. Specifically, discovering the algebraic relationships between state variables can give intuition about the nature of symmetries within the system and the natural coordinate system suitable for obtaining a simple model.

In all three cases presented here, SODAs identify the intrinsic algebraic constraints in the system, implying the reduced polar coordinate system inherent to it, solely based on pixel data that represents the time series of the pendulum's position in Cartesian coordinates (x, y) . For Cases 1 and 2, once the coordinate transformation is identified, the equation of the pendulum is discovered in the new transformed coordinate system.

System description.

A non-linear single pendulum with a mass attached to its end can be modeled using the following second-order ODE:

$$m\ddot{\omega} + \alpha\dot{\omega} + m\frac{g}{l}\sin\omega = 0, \quad (28)$$

where m and l represent the mass and length of the pendulum respectively, ω denotes the angle that the pendulum makes with the vertical axis, g represents the acceleration due to gravity, and α is the damping coefficient which takes the value of zero when damping is negligible. The physical constraint of the single pendulum can be captured by the equation

$$x^2 + y^2 = l^2, \quad (29)$$

where the transformations between the polar and Cartesian coordinates are given by:

$$x = l \sin \omega; \quad y = -l \cos \omega. \quad (30)$$

A double pendulum consists of two pendulums attached end to end, as shown in Figure 4a - *botom*. This assembly of two pendulums is well-studied and known to exhibit chaotic motion [64]. To simplify the analysis, we will neglect damping. The equations of motion for a double pendulum, derived using Lagrangian mechanics [64], are given by:

$$\ddot{\omega}_1 = \frac{g(\sin \omega_2 \cos(\omega_1 - \omega_2) - \mu \sin \omega_1) - (l_2 \dot{\omega}_2^2 + l_1 \dot{\omega}_1^2 \cos(\omega_1 - \omega_2)) \sin(\omega_1 - \omega_2)}{l_1(\mu - \cos^2(\omega_1 - \omega_2))}, \quad (31)$$

$$\ddot{\omega}_2 = \frac{g\mu(\sin \omega_1 \cos(\omega_1 - \omega_2) - \sin \omega_2) + (\mu l_1 \dot{\omega}_1^2 + l_2 \dot{\omega}_2^2 \cos(\omega_1 - \omega_2)) \sin(\omega_1 - \omega_2)}{l_2(\mu - \cos^2(\omega_1 - \omega_2))}, \quad (32)$$

where ω_1 and ω_2 denote the angles that the first and second pendulums make with the vertical axis, respectively, l_1, l_2 denote their respective lengths, m_1, m_2 denote their respective masses, and $\mu = 1 + \frac{m_1}{m_2}$. The physical constraints in this mechanical system are given by

$$x_1^2 + y_1^2 = l_1^2, \quad (33)$$

$$(x_1 - x_2)^2 + (y_1 - y_2)^2 = l_2^2, \quad (34)$$

where (x_1, y_1) and (x_2, y_2) denote the positions of the first and second pendulum in Cartesian coordinates. The transformations between the Cartesian and polar coordinate systems in this case are given by $x_1 = l_1 \sin \omega_1$, $y_1 = -l_1 \cos \omega_1$, $x_2 - x_1 = l_2 \sin \omega_2$, and $y_2 - y_1 = -l_2 \cos \omega_2$.

SODAs application.

For this study, pixel data from three different cases were used: 1) *single pendulum with negligible damping*: video recording of single pendulum experiments with negligible damping and three different initial conditions (Figure 4b - *left*), 2) *heavily damped pendulum*: video recording of animation of a heavily damped pendulum with four different initial conditions, 3) *chaotic double pendulum*: single video recording of the animation of a double pendulum exhibiting chaotic behavior (Figure 4b - *right*). Details about the collection of the pixel data and preprocessing can be found in supplementary Section 1.2.

An initial candidate library was constructed using monomials in the original states: $\Theta_1 = \{1, x, y, x^2, xy, \dots\}$ for Cases 1 and 2, and $\Theta_1 = \{1, x_1, y_1, x_2, y_2, x_1^2, \dots\}$ for Case 3. These choices were made under the assumption of lack of prior knowledge about the algebraic constraints present in the pixel data and further assuming that these constraints could be captured by a polynomial functions of the state variables. For the case of real-time experimental footage for case 1, monomials up to degree 3 were included in the candidate library. For case 2 and case 3 where we have better sampling of the state space compared to case 1, the highest monomial degree was varied between 2 and 5. A comparative study on the data requirement for equation discovery was carried out for the latter two cases (Figure 4c).

SODAs successfully discovered the constraint (29) for Cases 1 and 2. Note that $l = 1$ for our dataset due to the scaling of the pixel data. After discovering the constraint and identifying the reduced polar coordinate system, we applied the following transformation to move to the polar coordinate system:

$$x = l \cos \phi; \quad y = l \sin \phi, \quad (35)$$

where ϕ is the angle formed by the mass of the pendulum with the positive x -axis (Figure 4a - *top*). We made this choice instead of the natural one in(30) because, given (29), transformation (35) is the most straightforward coordinate transformation

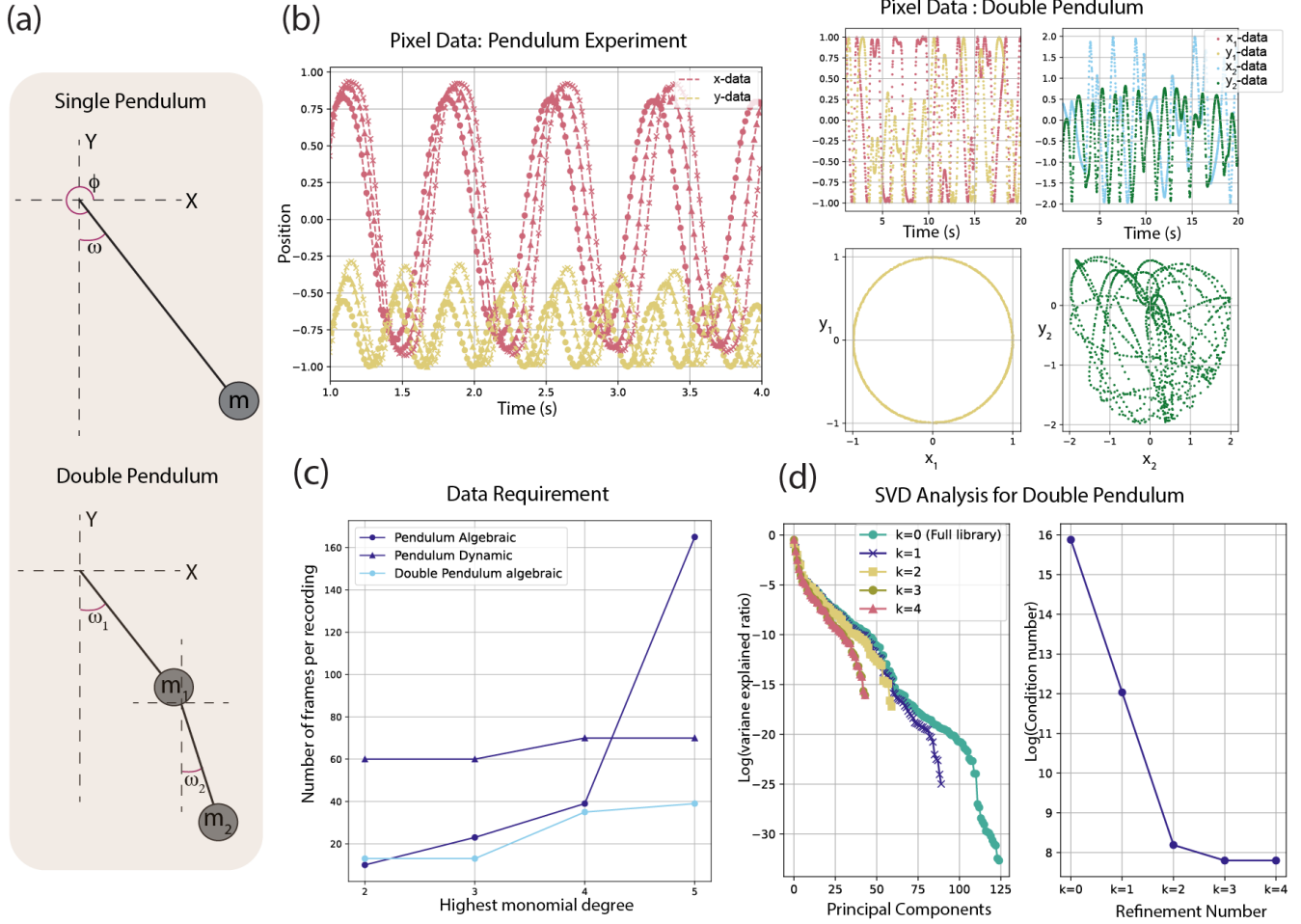


Figure 4. Example 3: Application to non-linear pendulum. (a) Schematic diagram: single pendulum (*top*) and double pendulum (*bottom*). (b) Scaled pixel data: single pendulum experiments (*left*) and double pendulum animation (*right*). (c) Data requirement: comparison between damped single pendulum and double pendulum. (d) SVD analysis: determining the number of algebraic constraints in the case of the chaotic double pendulum with degree 5 library.

in the absence of additional information about the system. Indeed, under the translation $\phi = \omega + \frac{3\pi}{2}$, it can be easily verified that the equations we discovered after applying the transformation (35) are consistent with (30) and (28). To discover the dynamic equations in the polar coordinate system, we applied a Savitzky-Golay filter [48] with a window size of 12 to compute the first and second derivatives of the ϕ . The candidate library consisted of monomials of $\phi, \dot{\phi}, \cos \phi$ and $\sin \phi$: $\Theta_* = \{\phi, \dot{\phi}, \cos \phi, \sin \phi, \phi^2, \phi \dot{\phi}, \dots\}$. Using (35), we included x and y in the library instead of calculating $\cos \phi$ and $\sin \phi$ directly from ϕ . Similar to the algebraic finder step, we restricted the monomial degree to 3 for Case 1 and varied it between 2 and 5 for Case 2 for a comparative study. After using sparse regression, where sequential threshold with inner iterations consisting of LASSO regularization was applied, we used a curve fit package to determine the correct parameters. In both case 1 and case 2, simulated solutions based on the discovered equations were able to predict the test pixel data accurately (see supplementary Section 3 for details on discovered equations and parameter estimation).

For Case 3, SODAs robustly identified the constraints (33)–(34) from pixel data obtained from a single video segment, using various upper bounds on the degree of the monomial library. Note that the polar nature of the states (x_2, y_2) is not immediately evident from the pixel data of the secondary pendulum in the double-pendulum (Figure 4b - right). This is because the secondary pendulum does not have a fixed pivot and sweeps trajectory in the 2D plane that doesn't correspond to an identifiable pattern. Nevertheless, SODAs discovered an expanded version of (34). This algebraic discovery enables us to determine the transformation to the polar coordinate system: $\phi_1 = \arctan \frac{y_1}{x_1}$ and $\phi_2 = \arctan \frac{y_1 - y_2}{x_1 - x_2}$, which can be further used for dynamic discovery. The dynamic discovery of equations governing the motion of the double pendulum similar to the form (31)–(32) based on polar coordinates, has been successfully demonstrated using SINDy-based methods [27]. We do not repeat this work here using our pixel data because it requires addressing noisy derivatives and may require advanced smoothing filters

to include higher-order derivatives of ϕ_1 and ϕ_2 in the candidate library. Instead, we use this example to demonstrate how SVD analysis, as discussed in Section 3, can be used to track the number of algebraic relationships present in the library and decide when to stop the library refinement in the algebraic finder step.

We used a Pareto front of the log of the condition number of the library to determine the stopping criterion. In Case 3, we stopped after two iterations as no further improvement in the condition number was observed from the third refinement onward (Figure 4d), implying the existence of two algebraic constraints. We also conducted a comparative study of the data requirement for Cases 2 and 3 as a function of maximum degree of the monomials in the candidate library (Figure 4c). The results indicate that the data requirement, in terms of the number of frames per video segment, stayed within manageable limits. Interestingly, the double pendulum required fewer frames per video segment for successful recovery of the algebraic equations compared to Case 2. This is because the chaotic nature of the pendulum, combined with a 3-minute-long video, provided a good sampling of the state space. We also shuffled the data points along the time axis only for Case 3 to ensure a good representation of the dynamics, given the longer length of the video segment. These factors contributed to the reduced data requirement in terms of the number of frames needed for successful recovery in Case 3. For Case 2, as the degree of the library reaches 5, the data requirement increases sharply. This can be attributed to the fact that higher-order terms in the library tend to be highly correlated when there is limited sampling of the state space. An alternative approach to reduce the number of frames required would be to conduct experiments with more informative initial conditions, which is closely related to experimental design [65, 66].

4.3 Example 3: Power-grid Dynamics

The operation of modern power grids relies on detailed modeling of dynamical behavior and network topology, which are critical for grid stability, efficiency, and control against disturbances [67]. Such model information directly supports daily operations, scheduling, and advanced techniques like state estimation, fault monitoring, and optimal power flow computation. However, the rise of renewable generation has led to decentralized power production, making detailed grid models less accessible in distribution systems due to frequent structural modifications. These include the addition and removal of network components and generating units, high uncertainty in distributed energy resources, line maintenance, faults, and other unplanned events. Yet, traditional power-grid monitoring and fault detection methods are often grounded on parameter estimation techniques, requiring extensive prior knowledge of grid configurations and physical properties [68–71]. The increasing deployment of phasor measurement units (PMUs) [72], capable of providing high-resolution data, offers a significant opportunity for automated model discovery [73, 74]. Here, we show that the sparse discovery of differential-algebraic models infers network topology robustly, which is encoded by the algebraic relationships among power levels at each bus. Using numerical results, we demonstrate that the proposed method accurately infers network models across a wide range of scenarios, including both small- and large-scale power grids, varying levels of state perturbation, and diverse PMU signal qualities.

System description.

The dynamics of power grids can be modeled as a network of coupled oscillators (nodes) interconnected through power transmission lines (links) [75–77]. The nodes correspond to conventional generators and consumers (geographically represented by substations and their attached load). In this representation, the dynamics of generators are governed by the swing equation [78]:

$$\frac{2H_i}{\omega_R} \ddot{\phi}_i + \frac{D_i}{\omega_R} \dot{\phi}_i = P_{m,i} - P_{e,i}, \text{ for } i = 1, \dots, n_g, \quad (36)$$

and the dynamics at the load buses and generator terminals follow the first-order phase oscillator model:

$$\frac{D_i}{\omega_R} \dot{\phi}_i = P_{\ell,i} - P_{e,i}, \text{ for } i = n_g + 1, \dots, N, \quad (37)$$

where n_g is the number of generators, n_ℓ is the number of load buses, and $N = 2n_g + n_\ell$ is the number of oscillators. The generator terminals correspond to buses at which generators are linked to the transmission system, acting as boundary points where the electrical output of the generators is delivered to the grid. Here, $\phi_i(t)$ is the phase angle of oscillator i at time t relative to the frame rotating at reference frequency $\omega_R = 2\pi f_R$, while H_i and D_i are the inertia and damping constants accounting for the mechanical properties of the generator. The supplied mechanical power by generators is $P_{m,i} > 0$, and the consumed power by loads is $P_{\ell,i} < 0$. For each bus $i = 1, \dots, N$, the electrical active power $P_{e,i}$ and reactive power $Q_{e,i}$ are determined by the system's conservation law (power flow) according to the following algebraic equations:

$$\begin{aligned} P_{e,i} &= + \sum_{j=1}^N |V_i V_j Y_{ij}| \sin(\phi_i - \phi_j - \gamma_{ij}), \\ Q_{e,i} &= - \sum_{j=1}^N |V_i V_j Y_{ij}| \cos(\phi_i - \phi_j - \gamma_{ij}), \end{aligned} \quad (38)$$

where V_i is the line voltage at bus i (assumed to be constant). The matrix entry $Y_{ij} = |Y_{ij}|e^{i(\gamma_{ij} + \frac{\pi}{2})}$ represents the admittance of the transmission line interconnecting buses (i, j) in polar form. Note that, at steady state, the system is balanced (i.e., $\sum_i P_{e,i} = 0$). For simplicity, we assume that the line's impedances are purely inductive (i.e., $\gamma_{ij} = 0$).

SODAs application.

We considered three IEEE benchmark cases with varying complexity (Figure 5a): IEEE-4, IEEE-9, and IEEE-39. Time series were generated under two distinct conditions: i) strong perturbations (Figure 5b - top), which excite nonlinear transient behaviors, and ii) weak perturbations (Figure 5b - bottom), suitable for small-signal stability analysis. We assume that the power grid is equipped with phasor measurement units (PMUs) placed on all N buses, providing us with high-resolution, high-frequency data for phase angle $\phi_i(t)$, frequency $\dot{\phi}_i(t)$, line voltage $V_i(t)$, and electrical power $P_{e,i}(t)$ and $Q_{e,i}(t)$. More information on network details, simulations and practicality of assumptions can be found in the supplementary Section 1.3.

SODAs was applied to the simulated time series to identify the network structure and parameters of the governing DAE system as described in equations (36)–(38). By using the well-established physical principles of power-grid dynamics, we achieved a significant advantage in constraining SODAs within a more informed framework. More specifically, the conservation of active power at each node leads to inherent algebraic constraints that we exploited to improve the identification process. In constructing the candidate library, we included the following functional forms: $P_{e,i}$ (active power states), ϕ_i (phase angles), ω_i (frequency), and sine terms of phase differences $\sin(\phi_i - \phi_j)$ for all pairs (i, j) . In a network with N nodes, this initial library included $3N + \frac{N(N+1)}{2}$ terms, which amounts to 39, 114, and 1,372 terms for the IEEE-4, IEEE-9, and IEEE-39 benchmarks, respectively. Additionally, by incorporating prior knowledge, we further reduced the number of candidate terms. For example, the conservation law involving $P_{e,i}$ at a given node i restricts the algebraic relations to include only sine terms of the form $\sin(\phi_i - \phi_j)$, for all nodes j . Using the `Daefiender.FeatureCouplingTransformer` class, we efficiently enforced these additional library constraints, minimizing computational complexity and enhancing the accuracy of identified models by eliminating irrelevant terms.

In the algebraic finder step, power laws constraining the active powers $P_{e,i}$ for all i are discovered (38). These power laws inherently reveal the power grid's network structure (encoded by the admittance matrix Y). In the dynamic finder step of SODAs, the differential equations governing the generators are discovered using a SINDy framework. We approximated the left-hand side of the dynamic equations (36)–(37) by utilizing derivatives of spline-fitted phase angles and applied sparse regression techniques, where LASSO was followed by sequential thresholding. Parameter estimation was subsequently performed through linear fitting with the discovered model structure. Note that for the identification of the dynamic equation, we modified the candidate library by removing the $\sin(\phi_i - \phi_j)$ terms, which had already been accounted for by the algebraic constraints. Instead, we incorporated state measurements of $P_{e,i}$ and hence reducing the number of candidate functions in the dynamic finder step from $3N + \frac{N(N+1)}{2}$ to $3N$. This refinement has also helped to avoid using the coupling terms $\sin(\phi_i - \phi_j)$, which have high sensitivity to noise in the data, for the dynamic finder step. We observed complete recovery of the true ODE system whenever the algebraic constraints were discovered with 100% accuracy. In contrast, attempts to identify coupled ODE equations without segregating the algebraic terms led to poor model recovery, even at SNR as high as 40dB, emphasizing the importance of this methodological separation of algebraic and differential equations.

We present SODAs' performance on identifying the ground-truth model for all three test cases, with a primary focus on the IEEE-39 benchmark test case (Figure 5c and 5d). We conducted similar analyses on the IEEE-4 and IEEE-9 benchmark networks, where SODAs demonstrated performance comparable or superior to that of the more complex IEEE-39 case. To evaluate the robustness of SODAs, we introduced varying amounts of noise into the simulated time-series data and examined performance across four different signal-to-noise ratios (SNR): no noise, 40 dB, 30 dB, and 20 dB. For each SNR level, we generated five distinct noise realizations and analyzed the performance as an average across these realizations. We found no significant variations in performance among the different noise realizations within the same SNR level, which allowed us to exclude error bars related to noise realizations in our figures.

The dynamics of the system are represented in the time series by the transients created from perturbations. Consequently, the number of perturbations reflects the amount of transient information about the system's dynamics. To evaluate SODAs' performance on this time-series dataset, we measured the percentage of true algebraic relationships recovered as a function of the number of perturbations in the time series. Additionally, to account for the variability in how the power grid responds to different random perturbations, we used ten different permutations of the perturbation order in our time-series simulations. We averaged the recovery performance over these ten permutations, representing the associated variability with error bars in our results.

For SNRs of no noise, 40 dB, and 30 dB, SODAs achieved 100% recovery of all algebraic relationships, as well as the dynamic ODEs, using the refined library for both small and large perturbations. Even under high noise conditions (SNR of 20 dB), SODAs maintained a recovery rate exceeding 80% for algebraic relations with 100 perturbations. The algebraic relationships related to power conservation at generator nodes were identified with relatively small number of perturbations,

underscoring the significant role of these nodes in influencing the overall dynamics of the power grid. Techniques such as signal averaging and advanced filtering can improve the SNR, even when the inherent measurement SNR is lower. Therefore, an SNR of 30 dB is assumed to be realistic for our further analysis, as other studies have reported PMU devices with signal quality at or above this level [79–82]. We evaluated the performance of SODAs at a 30 dB SNR across various benchmark cases and levels of perturbations (Figure 5d). We did a comparative analysis of the three benchmark cases, in terms of the number of perturbations required to recover all true DAE system components, and found that the number of perturbations required for full recovery increased with the complexity of the power grid, yet it remained within the realistic number of perturbations observed in practice (Figure 5d - left). Also, strong perturbations that induce significant transients in system dynamics enabled quicker recovery of the DAE system as expected (Figure 5d - right).

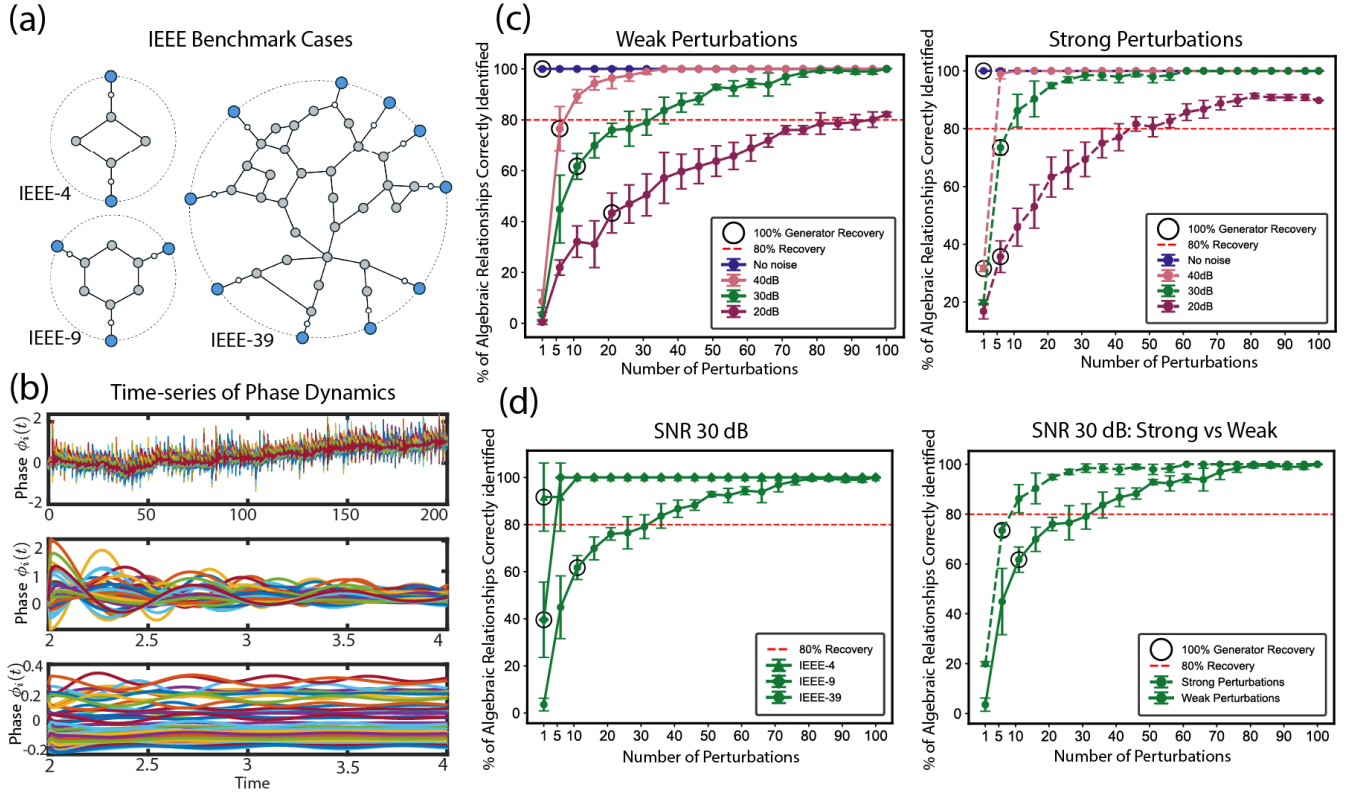


Figure 5. Discovery of power-grid networks. (a) Power-grid networks of the IEEE-4 (top left), IEEE-9 (bottom left), and IEEE-39 (right) benchmark systems. Generator buses are represented by blue nodes on the outer circle, while aggregated load buses are represented by gray nodes. (b) Time series of phase dynamics $\phi_i(t)$ for all nodes in the IEEE-39 power grid under different levels of perturbations: large perturbations (top), large perturbations zoomed-in (middle), and small perturbations zoomed-in (bottom). (c) Performance comparison of SODAs applied to IEEE-39 benchmark system across different SNR levels and : small perturbations (left) and large perturbations (right). (d) Performance comparison of SODAs at 30 dB SNR across: different benchmark cases (left) and different perturbation strengths (right).

5 Discussion

We have introduced SODAs as a method to discover DAEs from data in their explicit form, where the algebraic and differential components are identified separately. This separation played a crucial role in addressing the challenge of perfect multicollinearity within the candidate library, which often arises due to inbuilt algebraic relationships in a DAE system. Through an iterative refinement process, SODAs effectively reduces multicollinearity, ensuring robust and accurate discovery of governing equations. Separation of the algebraic and differential components of the DAE system also ensured that the potential noisy derivatives in the dataset do not affect the discovery of the algebraic component. Crucially, we have demonstrated the flexibility of SODAs by applying the method to three distinct applications. Our results show that SODAs is robust to noise and perform better than other SINDy-based implicit methods. We have also demonstrated that the data requirements for SODAs scale efficiently with the number of data points and the complexity of the library terms used.

There are several limitations and challenges worth pursuing in future work. One significant limitation of SODAs is the necessity to observe or measure all the state variables. In many physical systems, measuring all state variables can be challenging due to cost or physical infeasibility. Previous methods such as implicit-SINDy [26] and PI-SINDy [27] required no measurements of the algebraic states, but also assumed that all states were differential variables. Extending SODAs to discover DAEs even in the presence of unobserved states, potentially through recent strategies [19–21], would enable the identification of algebraic and differential variables and their equations when only a subset of states are measured. However, recovery in this setting will be even more challenging due to the non-convexity of sparse-optimization with hidden states as well as the potential lack of analytical identifiability in nonlinear DAE models [83].

One aspect of DAE discovery we did not yet explore is how SODAs performs when states are approximately but not fully in quasi-steady state. In realistic experimental sampling of systems with fast-slow variables, some transient dynamics may be sampled before the fast variables reach quasi-steady state. In this work, we used the reduced ODE formulation (24) of our CRNs to simulate the time series used for equation re-discovery, ensuring that the slow-variables were in perfect quasi-steady state. There was no error in the algebraic relationships since the algebraic variables were sampled during sufficiently short time interval of the transient regime. Future work is needed to investigate how SODAs performs as a function of sampling transient vs quasi-steady-state regimes for fast variables. An interesting avenue would be in mimicking the hybrid-SINDY approach [84, 85] in which a different model is selected when variables are in quasi-steady state.

There is a more general data limitation challenge inherent to sampling dynamical systems: sampling is often determined by the trajectories of the dynamics themselves which induces correlation between library terms. In cases where the available data does not adequately differentiate between lower-order and higher-order terms, strong correlations separate from the true algebraic relationships can occur. In Example 2, we showed how the data requirement increases as the degree of the monomial terms in the library increases to 5. This is attributed to the high correlation between higher-degree monomials in the library. This high correlation between library terms makes it challenging to separately identify their contributions to the dynamics of the system. This issue is not exclusive to SODAs; it is an inherent challenge in all SINDy-type methods that rely on sparse regression with function libraries. This challenge can be overcome by implementing improved data collection strategies or experimental design techniques [65, 66] that help with distinguishing different candidate library terms. We aim to develop methods to address these challenges in our future work. Finally, this study has focused on DAEs involving only ordinary derivatives, an exciting avenue for future research will be to extend SODAs to DAEs involving partial derivatives.

Data Accessibility.

All code and data used for numerical experiments in this paper are available at https://github.com/mjayadharan/DAE-FINDER_dev/tree/main/Examples. The `DaeFinder` package is also available through Python Package Index (PyPI) <https://pypi.org/project/DaeFinder>.

Authors' contributions.

M.J. developed the SODAs algorithm, implemented the `DaeFinder` package, and conducted all experiments (except for Example 1). C.C. contributed to the `DaeFinder` package and designed and conducted the numerical experiments in Example 1. A.N.M. designed the test cases and assisted in the numerical experiments in Example 3. N.M.M. designed and supervised the research. All authors edited the manuscript and approved the final draft for publication.

Competing Interests.

We have no competing interests.

Funding.

This material is based on work supported by several funding agencies. N. M. M. and M. J. were supported by the U.S. Department of Energy, Office of Science, Office of Advanced Scientific Computing Research, under Award Number DE-SC0024253 and Army Contracting Command under Award Number W52P1J-21-9-3023. C. C. was supported by the National Science Foundation under Grant No. DGS-2021900. Any opinions, findings, and conclusions or recommendations expressed in this material are those of the author(s) and do not necessarily reflect the views of the Department of Energy, Army Contracting Command, or National Science Foundation.

Acknowledgments.

We thank Finn Hagerty for his assistance in running simulations for the CRN example and related discussions.

References

1. Schmitt, M. S. *et al.* Machine learning interpretable models of cell mechanics from protein images. *Cell* **187**, 481–494.e24 (2024).
2. Amini, A. *et al.* Learning robust control policies for end-to-end autonomous driving from data-driven simulation. *IEEE Robotics Autom. Lett.* **5**, 1143–1150 (2020).

3. Taylor, A. T., Berrueta, T. A. & Murphey, T. D. Active learning in robotics: A review of control principles. *Mechatronics* **77**, 102576 (2021).
4. Higham, D. J. & Trefethen, L. N. Stiffness of odes. *BIT Numer. Math.* **33**, 285–303 (1993).
5. Shampine, L. F. & Gear, C. W. A user’s view of solving stiff ordinary differential equations. *SIAM review* **21**, 1–17 (1979).
6. Byrne, G. D. & Hindmarsh, A. C. Stiff ode solvers: A review of current and coming attractions. *J. Comput. physics* **70**, 1–62 (1987).
7. Mitchell, T. J. & Beauchamp, J. J. Bayesian variable selection in linear regression. *J. american statistical association* **83**, 1023–1032 (1988).
8. Miller, A. J. Selection of subsets of regression variables. *J. Royal Stat. Soc. Ser. A (General)* **147**, 389–425 (1984).
9. Bertsimas, D., King, A. & Mazumder, R. Best subset selection via a modern optimization lens. *The Annals Stat.* **44**, 813 – 852 (2016).
10. Brunton, S. L., Proctor, J. L. & Kutz, J. N. Discovering governing equations from data by sparse identification of nonlinear dynamical systems. *Proc. Natl. Acad. Sci.* **113**, 3932–3937 (2016).
11. Tibshirani, R. Regression shrinkage and selection via the lasso. *J. Royal Stat. Soc. Ser. B (Methodological)* **58**, 267–288 (2018).
12. Zou, H. & Hastie, T. Regularization and variable selection via the elastic net. *J. Royal Stat. Soc. Ser. B: Stat. Methodol.* **67**, 301–320 (2005).
13. Zheng, P., Askham, T., Brunton, S. L., Kutz, J. N. & Aravkin, A. Y. A unified framework for sparse relaxed regularized regression: Sr3. *IEEE Access* **7**, 1404–1423 (2019).
14. Sun, F., Liu, Y. & Sun, H. Physics-informed spline learning for nonlinear dynamics discovery. *arXiv preprint arXiv:2105.02368* (2021).
15. Van Breugel, F., Kutz, J. N. & Brunton, B. W. Numerical differentiation of noisy data: A unifying multi-objective optimization framework. *IEEE Access* **8**, 196865–196877 (2020).
16. Messenger, D. A. & Bortz, D. M. Weak sindy: Galerkin-based data-driven model selection. *Multiscale Model. & Simul.* **19**, 1474–1497 (2021).
17. Messenger, D. A. & Bortz, D. M. Weak sindy for partial differential equations. *J. Comput. Phys.* **443**, 110525 (2021).
18. Wentz, J. & Doostan, A. Derivative-based sindy (dsindy): Addressing the challenge of discovering governing equations from noisy data. *Comput. Methods Appl. Mech. Eng.* **413**, 116096 (2023).
19. Ribera, H., Shirman, S., Nguyen, A. & Mangan, N. Model selection of chaotic systems from data with hidden variables using sparse data assimilation. *Chaos: An Interdiscip. J. Nonlinear Sci.* **32** (2022).
20. Bakarji, J., Champion, K., Nathan Kutz, J. & Brunton, S. L. Discovering governing equations from partial measurements with deep delay autoencoders. *Proc. Royal Soc. A* **479**, 20230422 (2023).
21. Stepaniants, G., Hastewell, A. D., Skinner, D. J., Totz, J. F. & Dunkel, J. Discovering dynamics and parameters of nonlinear oscillatory and chaotic systems from partial observations. *Phys. Rev. Res.* **6**, 043062 (2024).
22. Lu, P. Y., Ariño Bernad, J. & Soljačić, M. Discovering sparse interpretable dynamics from partial observations. *Commun. Phys.* **5**, 206 (2022).
23. Nandakumar, A., Li, Y., Zhao, D., Zhang, Y. & Hong, T. Sparse identification-enabled data-driven modeling for nonlinear dynamics of microgrids. In *2022 IEEE Power & Energy Society General Meeting (PESGM)*, 1–5 (IEEE, 2022).
24. Nandakumar, A. *et al.* Data-driven modeling of microgrid transient dynamics through modularized sparse identification. *IEEE Transactions on Sustain. Energy* **15**, 109–122 (2023).
25. Sarić, A. T., Sarić, A. A., Transtrum, M. K. & Stanković, A. M. Symbolic regression for data-driven dynamic model refinement in power systems. *IEEE Transactions on Power Syst.* **36**, 2390–2402 (2020).
26. Mangan, N. M., Brunton, S. L., Proctor, J. L. & Kutz, J. N. Inferring biological networks by sparse identification of nonlinear dynamics. *IEEE Transactions on Mol. Biol. Multi-Scale Commun.* **2**, 52–63 (2016).
27. Kaheman, K., Kutz, J. N. & Brunton, S. L. Sindy-pi: a robust algorithm for parallel implicit sparse identification of nonlinear dynamics. *Proc. Royal Soc. A: Math. Phys. Eng. Sci.* **476**, 20200279 (2020).
28. França, T., Braga, A. M. B. & Ayala, H. V. H. Feature engineering to cope with noisy data in sparse identification. *Expert. Syst. with Appl.* **188**, 115995 (2022).

29. Kang, S. H., Liao, W. & Liu, Y. Ident: Identifying differential equations with numerical time evolution. *J. Sci. Comput.* **87**, 1 (2021).
30. He, Y., Kang, S.-H., Liao, W., Liu, H. & Liu, Y. Robust identification of differential equations by numerical techniques from a single set of noisy observation. *SIAM J. on Sci. Comput.* **44**, A1145–A1175 (2022).
31. Campbell, S., Ilchmann, A., Mehrmann, V., Reis, T. *et al.* *Applications of differential-algebraic equations: examples and benchmarks* (Springer, 2019).
32. Turanyi, T., Tomlin, A. & Pilling, M. On the error of the quasi-steady-state approximation. *The J. Phys. Chem.* **97**, 163–172 (1993).
33. Bothe, D. & Pierre, M. Quasi-steady-state approximation for a reaction–diffusion system with fast intermediate. *J. Math. Analysis Appl.* **368**, 120–132 (2010).
34. Brenan, K. E., Campbell, S. L. & Petzold, L. R. *Numerical Solution of Initial-Value Problems in Differential-Algebraic Equations*, chap. 2, 3,4, 15–114 (SIAM, 1995).
35. Rabier, P. J. & Rheinboldt, W. C. Theoretical and numerical analysis of differential-algebraic equations. In *Solution of Equations in R^n (Part 4), Techniques of Scientific Computing (Part4), Numerical Methods for Fluids (Part 2)*, vol. 8 of *Handbook of Numerical Analysis*, 183–540 (Elsevier, 2002).
36. Segel, L. A. & Slemrod, M. The quasi-steady-state assumption: a case study in perturbation. *SIAM review* **31**, 446–477 (1989).
37. Johnson, K. A. & Goody, R. S. The original michaelis constant: translation of the 1913 michaelis–menten paper. *Biochemistry* **50**, 8264–8269 (2011).
38. Srinivasan, B. A guide to the michaelis–menten equation: steady state and beyond. *The FEBS journal* **289**, 6086–6098 (2022).
39. Petzold, L. Differential/algebraic equations are not ode’s. *SIAM J. on Sci. Stat. Comput.* **3**, 367–384 (1982).
40. Kunkel, P. *Differential-algebraic equations: analysis and numerical solution*, vol. 2 (European Mathematical Society, 2006).
41. Ascher, U. & Petzold, L. R. *Computer Methods for Ordinary Differential Equations and Differential-Algebraic Equations* (SIAM, 1998).
42. de Silva, B. M. *et al.* Pysindy: A python package for the sparse identification of nonlinear dynamical systems from data. *J. Open Source Softw.* **5**, 2104 (2020).
43. Pathak, R. & Ma, C. On the design-dependent suboptimality of the lasso. *arXiv preprint arXiv:2402.00382* (2024).
44. James, G., Witten, D., Hastie, T., Tibshirani, R. *et al.* *An introduction to statistical learning*, vol. 112 (Springer, 2013).
45. Mangan, N. M., Kutz, J. N., Brunton, S. L. & Proctor, J. L. Model selection for dynamical systems via sparse regression and information criteria. *Proc. Royal Soc. A: Math. Phys. Eng. Sci.* **473**, 20170009 (2017).
46. Chakrabarti, A. & Ghosh, J. K. Aic, bic and recent advances in model selection. *Philos. statistics* 583–605 (2011).
47. Messenger, D. A. & Bortz, D. M. Asymptotic consistency of the w windy algorithm in the limit of continuum data. *arXiv preprint arXiv:2211.16000* (2022).
48. Bromba, M. U. & Ziegler, H. Application hints for savitzky-golay digital smoothing filters. *Anal. Chem.* **53**, 1583–1586 (1981).
49. Érdi, P. & Tóth, J. *Mathematical models of chemical reactions: theory and applications of deterministic and stochastic models* (Manchester University Press, 1989).
50. Alon, U. *An introduction to systems biology: design principles of biological circuits* (Chapman and Hall/CRC, 2019).
51. Bowen, J., Acrivos, A. & Oppenheim, A. Singular perturbation refinement to quasi-steady state approximation in chemical kinetics. *Chem. Eng. Sci.* **18**, 177–188 (1963).
52. Goeke, A., Schilli, C., Walcher, S. & Zerz, E. Computing quasi-steady state reductions. *J. Math. Chem.* **50**, 1495–1513 (2012).
53. Snowden, T. J., van der Graaf, P. H. & Tindall, M. J. Methods of model reduction for large-scale biological systems: a survey of current methods and trends. *Bull. mathematical biology* **79**, 1449–1486 (2017).
54. Bhattacharya, K., Hosseini, B., Kovachki, N. B. & Stuart, A. M. Model Reduction And Neural Networks For Parametric PDEs. *The SMAI J. computational mathematics* **7**, 121–157 (2021).

55. Benner, P., Goyal, P., Kramer, B., Peherstorfer, B. & Willcox, K. Operator inference for non-intrusive model reduction of systems with non-polynomial nonlinear terms. *Comput. Methods Appl. Mech. Eng.* **372**, 113433 (2020).
56. Mills, C. E. *et al.* Vertex protein pdun tunes encapsulated pathway performance by dictating bacterial metabolosome morphology. *Nat. communications* **13**, 3746 (2022).
57. Kennedy, N. W. *et al.* Linking the salmonella enterica 1, 2-propanediol utilization bacterial microcompartment shell to the enzymatic core via the shell protein pdub. *J. bacteriology* **204**, e00576–21 (2022).
58. Bartha, R. Effect of signal-to-noise ratio and spectral linewidth on metabolite quantification at 4 t. *NMR Biomed. An Int. J. Devoted to Dev. Appl. Magn. Reson. In vivo* **20**, 512–521 (2007).
59. Meyer, C. *et al.* Minimum required signal-to-noise ratio for optimal precision in hplc and ce. *Electrophoresis* **33**, 1509–1516 (2012).
60. Yang, Q., Sing-Long, C. A. & Reed, E. J. L1 regularization-based model reduction of complex chemistry molecular dynamics for statistical learning of kinetic monte carlo models. *MRS Adv.* **1**, 1767–1772 (2016).
61. Wen, M. *et al.* Chemical reaction networks and opportunities for machine learning. *Nat. Comput. Sci.* **3**, 12–24 (2023).
62. Mars Gao, L. & Nathan Kutz, J. Bayesian autoencoders for data-driven discovery of coordinates, governing equations and fundamental constants. *Proc. Royal Soc. A* **480**, 20230506 (2024).
63. Yang, J., Dehmamy, N., Walters, R. & Yu, R. Latent space symmetry discovery. *arXiv preprint arXiv:2310.00105* (2023).
64. Shinbrot, T., Grebogi, C., Wisdom, J. & Yorke, J. A. Chaos in a double pendulum. *Am. J. Phys.* **60**, 491–499 (1992).
65. Seltman, H. J. *Experimental design and analysis* (2012).
66. Versyck, K. J., Bernaerts, K., Geeraerd, A. H. & Van Impe, J. F. Introducing optimal experimental design in predictive modeling: A motivating example. *Int. J. Food Microbiol.* **51**, 39–51 (1999).
67. Gong, X., Wang, X. & Cao, B. On data-driven modeling and control in modern power grids stability: Survey and perspective. *Appl. Energy* **350**, 121740 (2023).
68. Pierre, J. W. *et al.* Overview of system identification for power systems from measured responses. *IFAC Proc. Vol.* **45**, 989–1000 (2012).
69. Gopakumar, P., Mallikajuna, B., Reddy, M. J. B. & Mohanta, D. K. Remote monitoring system for real time detection and classification of transmission line faults in a power grid using pmu measurements. *Prot. Control. Mod. Power Syst.* **3**, 1–10 (2018).
70. Liu, Y. *et al.* Dynamic state estimation for power system control and protection. *IEEE Transactions on Power Syst.* **36**, 5909–5921 (2021).
71. Gaskin, T., Pavliotis, G. A. & Girolami, M. Inferring networks from time series: A neural approach. *PNAS nexus* **3**, pgae063 (2024).
72. Rodrigues, Y. R., Abdelaziz, M., Wang, L. & Kamwa, I. Pmu based frequency regulation paradigm for multi-area power systems reliability improvement. *IEEE Transactions on Power Syst.* **36**, 4387–4399 (2021).
73. Ardakanian, O. *et al.* On identification of distribution grids. *IEEE Transactions on Control. Netw. Syst.* **6**, 950–960 (2019).
74. Yuan, Y. *et al.* Data driven discovery of cyber physical systems. *Nat. communications* **10**, 4894 (2019).
75. Sadamoto, T., Chakraborty, A., Ishizaki, T. & Imura, J.-i. Dynamic modeling, stability, and control of power systems with distributed energy resources: Handling faults using two control methods in tandem. *IEEE Control. Syst. Mag.* **39**, 34–65 (2019).
76. Dörfler, F., Chertkov, M. & Bullo, F. Synchronization in complex oscillator networks and smart grids. *Proc. Natl. Acad. Sci.* **110**, 2005–2010 (2013).
77. Nishikawa, T. & Motter, A. E. Comparative analysis of existing models for power-grid synchronization. *New J. Phys.* **17**, 015012 (2015).
78. Saadat, H. *Power system analysis*, vol. 2 (McGraw-Hill, 1999).
79. Brown, M., Biswal, M., Brahma, S., Ranade, S. J. & Cao, H. Characterizing and quantifying noise in pmu data. In *IEEE Power and Energy Society General Meeting* (2016).
80. Bhandari, A., Yin, H., Liu, Y., Yao, W. & Zhan, L. Real-time signal-to-noise ratio estimation by universal grid analyzer. In *International Conference on Smart Grid Synchronized Measurements and Analytics* (2019).

81. Frigo, G., Derviškić, A., Bach, A. & Paolone, M. Statistical model of measurement noise in real-world pmu-based acquisitions. In *International Conference on Smart Grid Synchronized Measurements and Analytics* (2019).
82. Zhang, X., Lu, C., Lin, J. & Wang, Y. Experimental test of pmu measurement errors and the impact on load model parameter identification. *IET Gener. Transm. & Distribution* **14**, 4593–4604 (2020).
83. Montanari, A. N., Lamoline, F., Bereza, R. & Gonçalves, J. Identifiability of differential-algebraic systems. *arXiv:2405.13818* (2024).
84. Mangan, N. M., Askham, T., Brunton, S. L., Kutz, J. N. & Proctor, J. L. Model selection for hybrid dynamical systems via sparse regression. *Proc. Royal Soc. A* **475**, 20180534 (2019).
85. Li, Y., Wu, K. & Liu, J. Discover governing differential equations from evolving systems. *Phys. Rev. Res.* **5**, 023126 (2023).
86. Bradski, G. & Kaehler, A. *Learning OpenCV: Computer vision with the OpenCV library* (" O'Reilly Media, Inc.", 2008).
87. Zimmerman, R. D., Murillo-Sánchez, C. E. & Thomas, R. J. Matpower: Steady-state operations, planning, and analysis tools for power systems research and education. *IEEE Transactions on Power Syst.* **26**, 12–19 (2010).
88. Peng, J., Sun, Y. & Wang, H. Optimal pmu placement for full network observability using tabu search algorithm. *Int. J. Electr. Power & Energy Syst.* **28**, 223–231 (2006).
89. Gou, B. & Kavasseri, R. G. Unified pmu placement for observability and bad data detection in state estimation. *IEEE Transactions on Power Syst.* **29**, 2573–2580 (2014).
90. Montanari, A. N. & Aguirre, L. A. Observability of network systems: A critical review of recent results. *J. Control. Autom. Electr. Syst.* **31**, 1348–1374 (2020).

Supplementary Material

1 Time series generation and Data processing

1.1 Example 1: Chemical Reaction Networks

Time series for three different CRNs were generated by solving equations of the simplified form (24). Note that this means that the algebraic relationships induced by quasi-steady-state approximations are strictly enforced. CRN1 is the simple Michealis-Menten reaction, CRN2 is the competition of two enzymes for a shared substrate, and CRN3 is the simplified propanediol utilization pathway. These reactions are:

1. CRN1: 1 reaction, 4 states including complex and enzyme
2. CRN2: 2 reactions, 7 states including complexes and enzymes
3. CRN3: 4 reactions (one reversible), 14 states including complexes and enzymes

CRN1 and CRN2 are nested within CRN3, with CRN3 chaining CRN1 and a modified CRN2 with an additional reaction consuming one of CRN2's products. CRN3 also complicates the simple, irreversible reaction mechanism of CRN1 and CRN2, and one reaction is made reversible to mimic the current understandings of the true propanediol utilization pathway. In function, reversibility can be thought of as having the effect of an additional reaction.

Simulations for each CRN consisted of five initial conditions, each simulated to a fixed end time ($t = 4$ for CRN1 & CRN2, $t = 10$ for CRN3; Figure 3a). Within each CRN, initial enzyme concentrations were fixed between simulations, while initial substrate concentrations were selected to be equally spaced within a given range for each species (fixed for CRN1 & CRN2, set by reasonable experimental ranges for CRN3). Such a selection was intended to effectively sample the breadth of system behaviors that result from all possible initial conditions. Model parameters for CRN1 and CRN2 were chosen to meet the assumptions required for the quasi-steady-state approximation made in deriving Michaelis-Menten kinetics to be reasonable (i.e., that binding is much faster than unbinding and that initial substrate concentration far exceeds enzyme concentration) [37, 38]. Parameters for CRN3 were taken from the literature [57].

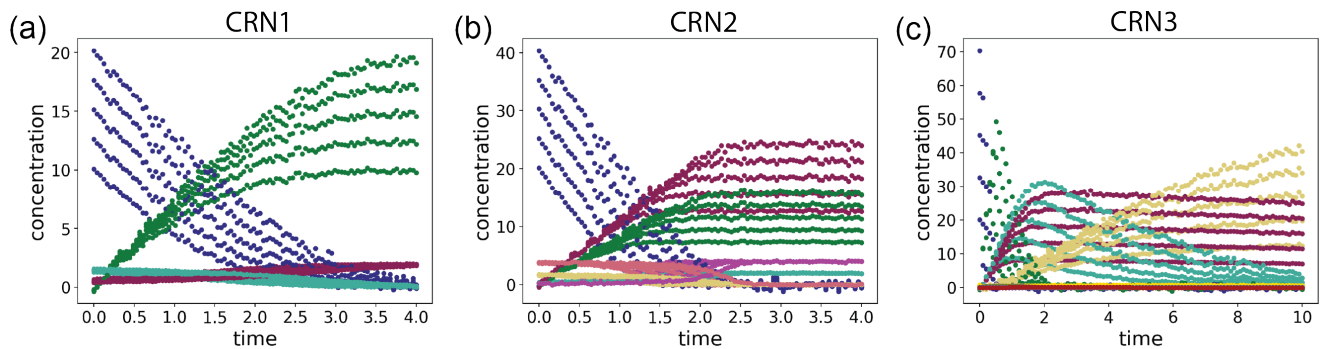


Figure 6. CRN simulated time series: Five initial conditions simulated for each CRN at 1% noise with 100 data points per initial condition. Colored by species. (a) CRN1, (b) CRN2, (c) CRN3.

To mimic possible measurement error present in real-world data and to test noise robustness of the SODAs algorithm, Gaussian noise of up to 15% was added to the simulated time series according to (20) prior to the application of SODAs. In addition, we applied SODAs across a varied sampling resolution, simulating uniform grids in t with 5-1200 data points per initial condition for all CRNs. This is equivalent to $\Delta t \in \{0.00\bar{3}, 0.8\}$ for CRN1 and CRN2, and to $\Delta t \in \{0.008\bar{3}, 2\}$ for CRN3. Examples of the simulated time series from each CRN used to assess the SODAs algorithm are shown in Figure 6.

1.2 Example 2: Non-linear and Chaotic Pendulum

1. Single pendulum experiments with negligible damping: Three separate experiments were conducted in which a single pendulum was swung from different initial positions and with varying initial velocities (Figure 4b - left). The initial conditions were chosen to ensure that small-angle or linear approximations were no longer valid. The experiments were recorded at 120 frames per second (fps), for a duration of 20 seconds. The recordings were made when the damping was minimal.

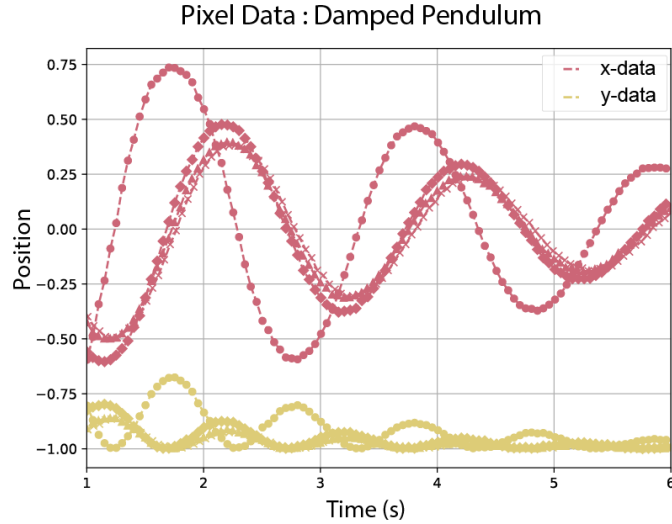


Figure 7. Damped pendulum: scaled pixel data.

2. Heavily damped pendulum: Four different video clips of animation of a heavily damped pendulum were recorded at 60 fps, each lasting 20 seconds (Figure 7). Each clip captured various behaviors based on different initial conditions.
3. Chaotic double pendulum: A single video recording of the animation of a double pendulum (Figure 4b - right) exhibiting chaotic behavior at 60 fps was used. The recording lasted for 3 minutes. Both pendulums have equal length and the same masses attached to the end. Due to the chaotic and non-repetitive behavior of the system, this single initial condition provided a good sampling of various regions in the phase space.

In all three cases, the OpenCV [86] package in Python was used to extract the pixel data from the video recordings. A combination of color- and motion-based sensing was used to track the masses of the pendulums and obtain their Cartesian coordinates. The raw pixel data was centered and scaled such that the origin was positioned at the pivot of the single pendulum and at the pivot of the primary pendulum in the double pendulum case. The scaling ensured that the length of the pendulum is 1. These preprocessing steps were performed to normalize the features and minimize unnecessary cross-terms in the discovered equations, even though we verified that SODAs could discover the correct equations without centering and scaling the pixel data. The raw footage and processed data sets used in this example are available at https://github.com/mjayadharan/DAE-FINDER_dev/tree/main/Examples/Example_2_pendulum/data.

1.3 Example 3: Power-grid Dynamics

We consider the following cases available through MATPOWER toolbox [87]:

1. IEEE-4 benchmark: 2 generators and 4 buses.
2. IEEE-9 benchmark: 3 generators and 9 buses.
3. IEEE-39 benchmark: 10 generators and 39 buses.

The IEEE-39 is a simplified representation of the New England section of the Eastern Interconnection in the North American power grid, where a single generator represents the link to the remainder of the grid. Each generator is associated to a terminal, represented as a white node, which acts as an interconnection point to the rest of the grid. The simulations include the nominal voltage magnitudes V_i , load consumption $P_{\ell,i}$, and admittance matrices Y . The generator-supplied power $P_{m,i}$ as well as the electrical power $P_{e,i}$ are derived from the AC power flow solution. The generator and load dynamic parameters, H_i and D_i , are estimated using the approach described in [77], with the nominal frequency $f_R = 60$ Hz. The power flow equations are solved numerically using the MATPOWER toolbox [87]. The initial conditions assume that the power system is in a synchronized steady state, i.e., $\dot{\phi}_i(0) = 0, \forall i$, with $\phi_i(0)$ determined by the power flow solution.

We numerically simulated the system over the time interval $t \in [0, 100]$ s, introducing a random perturbation $v_i(t) \sim \mathcal{N}(0, \sigma^2)$ to the system state $\phi_i(0)$ every 2s. This setup mimics the transient response of power grids to random fluctuations, such as changes in load demand, generation, or minor faults. Perturbations are added at regular time intervals (rather than irregularly or continuously) to ensure consistent excitation across time, allowing us to assess the performance of SODAs based

on the length of the time-series measurements. Strong and weak perturbations corresponds to $\sigma = 0.5$ and $\sigma = 0.1$ respectively. We assume that the power grid is equipped with phasor measurement units (PMUs) placed on all N buses, providing us with high-resolution, high-frequency data for phase angle $\phi_i(t)$, frequency $\dot{\phi}_i(t)$, line voltage $V_i(t)$, and electrical power $P_{e,i}(t)$ and $Q_{e,i}(t)$. While this assumption simplifies data availability and ensures state observability [88–90], it may not be entirely practical for all power grids (particularly those with limited infrastructure or cost constraints, as PMUs are often expensive and not yet deployed universally). However, the increasing adoption of smart-grid technologies and improved data acquisition systems are gradually making this level of measurement more feasible in modern grids [72].

2 CRN Example Details

2.1 Model definition

By the structure presented in Section 4.1, CRN models are defined by a stoichiometry matrix \mathbf{S} and reaction rate vector $\mathbf{v}(\mathbf{x})$. Quasi-steady-state approximations allow a reduced system to be represented in terms of only its slow variables \mathbf{z} . For completeness, we give \mathbf{S}_z and $\mathbf{v}(\mathbf{g}(\mathbf{z}), \mathbf{z})$ for each CRN where $K_{MN} = \frac{k_{-N} + k_{\text{cat},N}}{k_N}$.

CRN1

We assume that AE_1 (and by extension, E_1 due to mass conservation) is at quasi-steady state, yielding:

$$\mathbf{S}_z = \begin{bmatrix} -1 \\ 1 \end{bmatrix} \quad \mathbf{v}(\mathbf{g}(\mathbf{z}), \mathbf{z}) = \begin{bmatrix} \frac{k_{\text{cat},1}E_1^{\text{tot}}[A]}{K_{M1}+[A]} \end{bmatrix}$$

CRN2

We assume that BE_2 and BE_3 (and by extension, E_2 and E_3) are at quasi-steady state, yielding:

$$\mathbf{S}_z = \begin{bmatrix} -1 & -1 \\ 1 & 0 \\ 0 & 1 \end{bmatrix} \quad \mathbf{v}(\mathbf{g}(\mathbf{z}), \mathbf{z}) = \begin{bmatrix} \frac{k_{\text{cat},2}E_2^{\text{tot}}[B]}{K_{M2}+[B]} \\ \frac{k_{\text{cat},3}E_3^{\text{tot}}[B]}{K_{M3}+[B]} \end{bmatrix}$$

CRN3

We assume that AE_1 , BE_2 , BE_3 , and DE_4 (and by extension, E_1 , E_2 , E_3 and E_4) are at quasi-steady state, yielding:

$$\mathbf{S}_z = \begin{bmatrix} -1 & 0 & 0 & 0 \\ 1 & -1 & -1 & 0 \\ 0 & 1 & 0 & 0 \\ 0 & 0 & 1 & -1 \\ 0 & 0 & 0 & 1 \end{bmatrix} \quad \mathbf{v}(\mathbf{g}(\mathbf{z}), \mathbf{z}) = \begin{bmatrix} \frac{k_{\text{cat},1}E_1^{\text{tot}}[A]}{K_{M1}+[A]} \\ \frac{k_{\text{cat},2}E_2^{\text{tot}}[B]}{K_{M2,f}+[B] + \left(\frac{K_{M2,f}}{K_{M2,r}}\right)[C]} \\ \frac{k_2E_2^{\text{tot}}[C]}{K_{M2,r}+[C] + \left(\frac{K_{M2,r}}{K_{M2,f}}\right)[B]} \\ \frac{k_{\text{cat},3}E_3^{\text{tot}}[B]}{K_{M3}+[B]} \\ \frac{k_{\text{cat},4}E_4^{\text{tot}}[D]}{K_{M4}+[D]} \end{bmatrix}$$

Note here that due to reversibility of the reaction catalyzed by E_2 (green arrow; Figure 3a), v_2 and v_3 contain a more complex denominator term than their equivalent reactions nested in CRN2.

2.2 Non-monotonicity in rediscovery

We were interested in guarantees about data quantity and quality for SODAs success, guiding our choice of definition for SODAs' data requirement. The choice of this requirement as the resolution above which SODAs always succeeded in recovering true algebraic relationships up to a tested total of 1200 data points per initial condition was also motivated by the fact that recovery appears non-monotonic for a given random seed as the resolution increased up until a certain point. Generally, for low resolutions, recovery was possible, but was subject to the stochasticity introduced by noise. As data increased, recovery became less dependent on a single noise instance. This is what our definition aimed to capture. Examples of non-monotonicity in the discovery of CRN1 are shown for various noise in Figure 8.

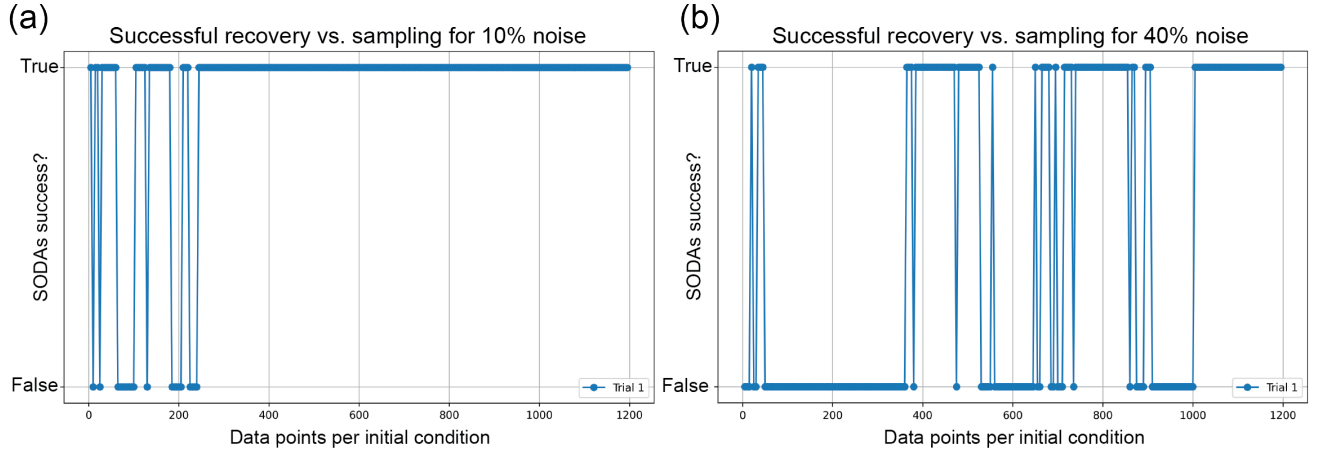


Figure 8. Non-monotonic scaling of CRN1 rediscovery with increasing resolution: (a) Recovery pattern for Trial 1 of 10 for 10% noise shows initial monotonicity before resolving at approximately 250 data points per initial condition, (b) Recovery pattern for Trial 1 of 10 for 40% noise; while 40% noise was not included in our scaling study, it is demonstrative of how the recovery pattern can change as noise is increased.

2.3 SVD and Pareto front analysis

The use of SVD and Pareto front analysis was critical to setting the stopping criterion for library refinement (see Section 3). We include this analysis for CRN1 in the main text in Figure 2. The same analysis is included here for CRN2 and CRN3 in Figure 9. This suggested a stopping criterion of three refinements for CRN2 and five refinements for CRN3.

2.4 CRN1: Discovered vs. True Model

In testing a single seed at 0%, 5%, and 15% noise, after correct identification of algebraic relationships, we find

$$\frac{d[A]}{dt} = -\frac{d[B]}{dt} = -4.99[AE_1], \quad (39)$$

$$\frac{d[A]}{dt} = -\frac{d[B]}{dt} = -5.02[AE_1], \quad (40)$$

$$\frac{d[A]}{dt} = -\frac{d[B]}{dt} = -5.07[AE_1] \quad (41)$$

respectively after refitting (Figure 10). This is a result sufficiently close to the true coefficient of 5.00. We note that when recovery failed, its failures were consistent and a small coefficient was regularly learned in addition to the structure in (39)–(41). We may anticipate that the use of information criteria to determine the optimal sparsity of learned models across a variety of sparsity parameters in LASSO may help distinguish and select among model structures that appear similar.

3 Pendulum: Discovered vs. True Model

We used `scipy.optimize.curve_fit` function for parameter estimation to determine the correct parameters after SODAs discovered the functional form of the ODEs for the single pendulum. For Case 1, the final discovered solution with optimized parameters is as follows:

$$\ddot{\phi} = -82.9 \cos \phi. \quad (42)$$

For Case 2 with non-zero damping, the final discovered solution with optimized parameters is as follows:

$$\ddot{\phi} = -0.47\dot{\phi} - 9.73 \cos \phi. \quad (43)$$

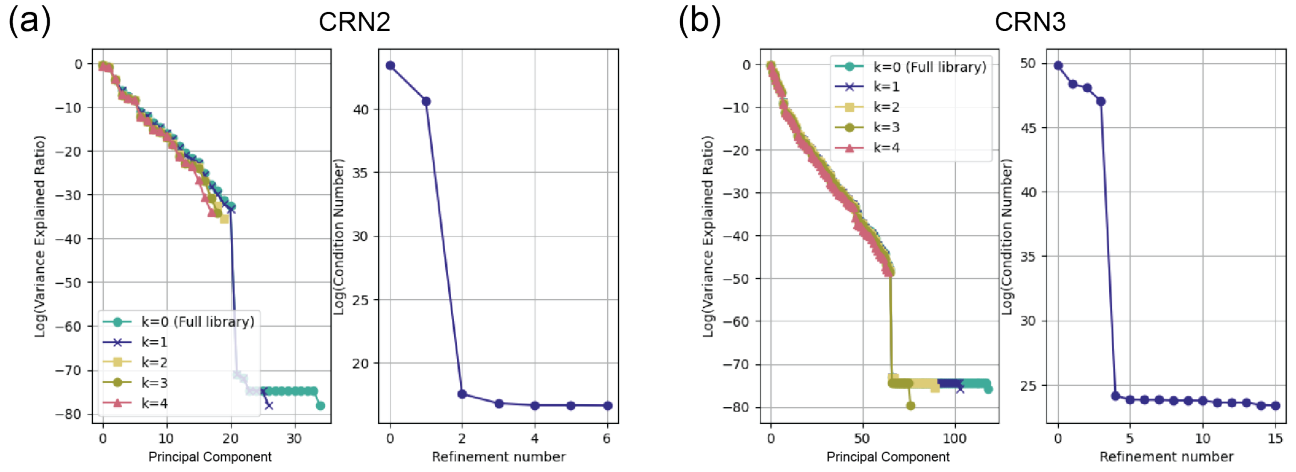


Figure 9. SVD and Pareto front analysis for CRN2 and CRN3: (a) SVD and Pareto front for CRN2 with 1000 data points per initial condition, 0% noise, and $p = 2$, (b) SVD and Pareto front for CRN3 with 1000 data points per initial condition, 0% noise, and $p = 2$.

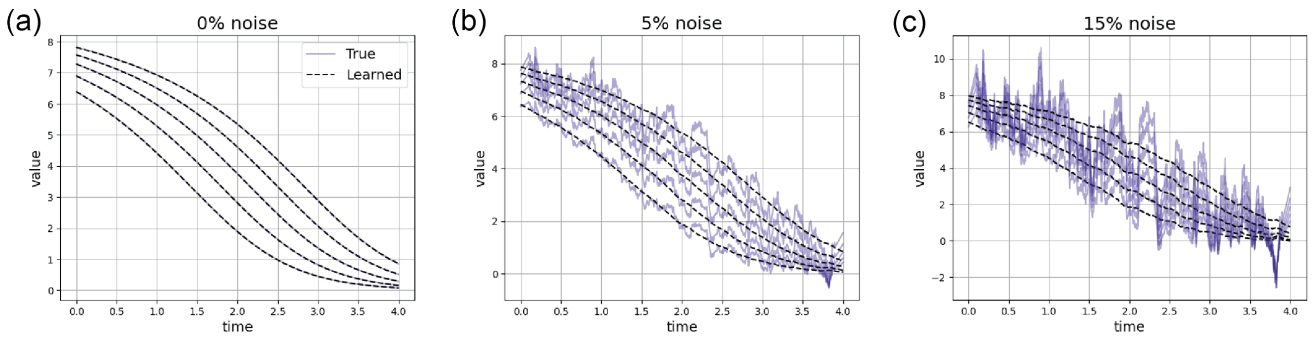


Figure 10. Results of CRN1 discovery: Estimation of $\frac{d[A]}{dt}$ for all tested initial conditions with learned coefficient for $[AE_1]$ applied to simulated data of 1000 data points per initial condition and $p = 2$ (a) (39) is the result of discovery at 0% noise, (b) (40) is the result of discovery at 5% noise, (c) (41) is the result of discovery at 15% noise.

In both cases, simulated solutions based on the discovered equations (42) (Figure 11a) and (43) (Figure 11b) closely aligned with the corresponding training data as well as the remaining processed pixel data. Note that in both cases, the discovered equations (42) and (43) are equivalent to (28) under the translation $\phi = \omega + \frac{3\pi}{2}$, for the cases of zero and non-zero damping, respectively. Note that for Case 1, the parameter -82.9 corresponds to $-\frac{g_{\text{modified}}}{l_{\text{modified}}}$, where g_{modified} represents the modified acceleration due to gravity, and l_{modified} is the scaled length of the pendulum. Scaling the pixel data involved enforcing $l_{\text{modified}} = 1$, which altered the length of the pendulum while preserving the time period. This adjustment resulted in a modified acceleration due to gravity, g_{modified} , in the classical sense. However, for Case 2, since the original pendulum animation depicted a pendulum of length 1, we were able to obtain a parameter very close to the actual acceleration due to gravity g .

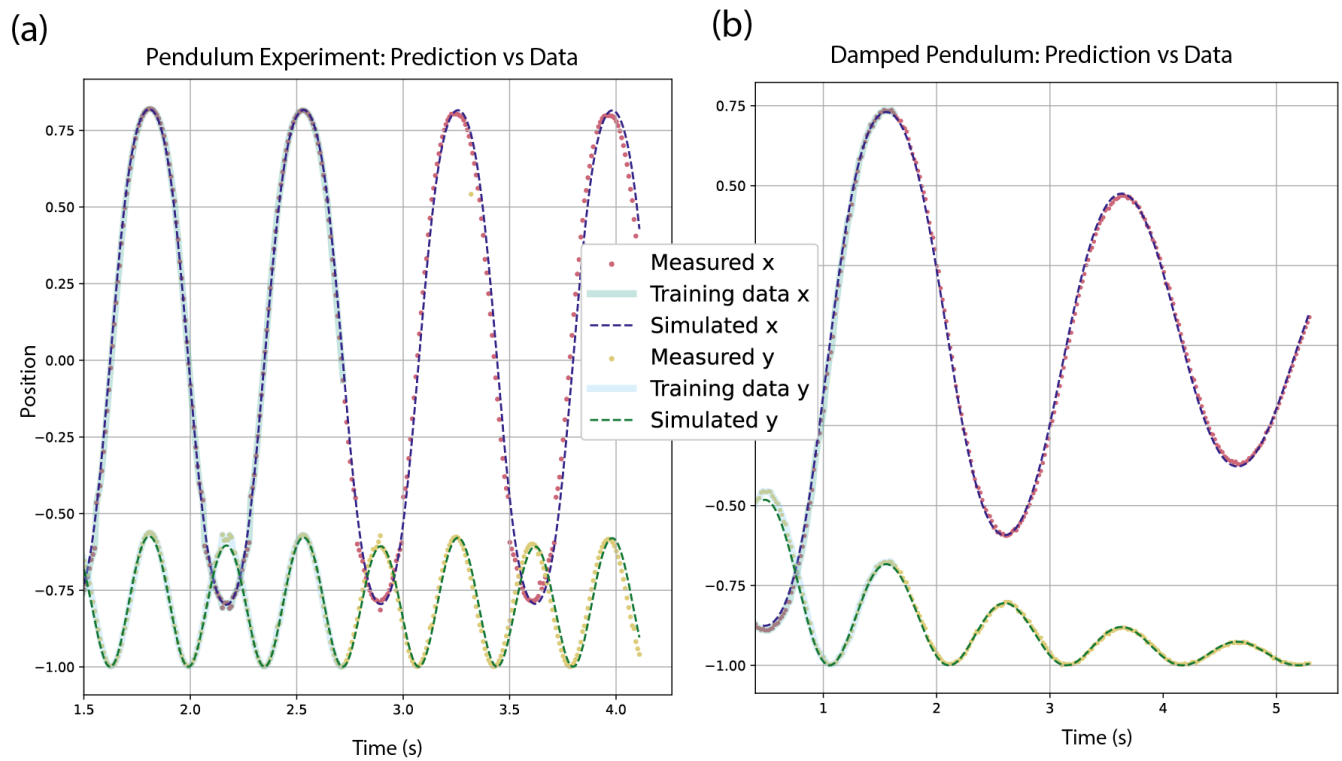


Figure 11. Prediction based on the discovered model using SODAs: (a) pendulum experiment with negligible damping, (b) heavily damped pendulum animation. In both cases, the highlighted region shows the training data. The simulated solution based on the discovered model matches closely with the entirety of the available data showing good prediction capability.